Electronic Supplementary Information

In-situ bulk hydrogen intercalation in mirror-symmetric Ru/WO_{3-x} nanoarray boosts neutral electrocatalytic nitrate reduction to ammonia

Hongchuan Fu,‡[ab] Song Lu,‡[c] Yu Xin,[ab] Shoukang Xiao,[ab] Liyu Chen,[ab] Yingwei Li[ab] and Kui Shen[ab]*

[a] Guangdong Provincial Key Laboratory of Fuel Cell Technology, School of Chemistry and Chemical Engineering, South China University of Technology, Guangzhou 510641, China.
[b] Guangdong Provincial Key Lab of Green Chemical Product Technology, School of Chemistry and Chemical Engineering, South China University of Technology, Guangzhou 510640, China.
[c] Institute of New Energy, School of Chemistry and Chemical Engineering, Shaoxing University, Shaoxing 312000, China.

‡ These authors contributed equally to this work.

*Corresponding author.

E-mail: cekshen@scut.edu.cn

Experimental Details

Materials. Ammonium metatungstate ($(NH_4)_6H_2W_{12}O_{40}\cdot xH_2O$, AMT, 99.5%), was purchased from Alfa Aesar. Ruthenium(III) chloride hydrate ($RuCl_3$, 99.5%), maleic acid ($C_4H_4O_4$, 99%), dimethyl sulfoxide-d6 (C_2D_6OS, 99.9%), and 5wt % Ru/C were obtained from Innochem. Potassium nitrate (KNO_3, 99%), ammonium chloride (NH_4Cl, 99%), sodium hypochlorite solution (NaClO, 6-14% active chlorine), potassium nitrite (KNO_2, 97%), sodium citrate ($C_6H_5Na_3O_7$, 98%), potassium phosphate monobasic (KH_2PO_4, 99%), potassium sulfate (K_2SO_4, 99%), potassium hydroxide (KOH, 95%), phosphoric acid (H_3PO_4, ≥ 85 wt.% in H_2O, ρ = 1.70 g/mL), N-(1-naphthyl)ethylenediamine dihydrochloride ($C_{12}H_{14}N_2\cdot 2HCl$, 98%), salicylic acid ($C_7H_6O_3$, 99.5%), sodium nitroprusside ($C_5FeN_6Na_2O$, 99%), and sulfanilamide ($C_6H_8N_2O_2S$, 99%) were supplied by Aladdin. Potassium nitrate-^{15}N (KNO_3, 98.5%) and ammonium chloride-^{15}N ($^{15}NH_4Cl$, 98.5%) were bought from Macklin. Ni foam (NF, thickness: 1.0 mm) was purchased from Saibo Electronics. Carbon cloth (CC; thickness: 1.0 mm) was purchased from CeTech. All chemicals were used as received without further purification. Ultrapure water (18.2 MΩ cm) was used throughout the experiments.

Preparation of the mirror-symmetric WO_3 nanoarray. A uniformly distributed mirror-symmetric WO_3 nanoarray (MSN-WO_3) was prepared on NF by a facile hydrothermal process. The purchased NF was first tailored as 3 cm × 4 cm, and the tailed NF was sonicated with acetone and 3 M HCl individually to remove surface impurities. Then, 0.6 mmol AMT was added to 65 mL of deionized water. The above mixture containing the pretreated NF sealed in a 100 mL Teflon-lined autoclave was heated at 170 °C for 10 h, and the resultant MSN-WO_3 was rinsed with copious absolute ethanol and dried naturally.

Preparation of the mirror-symmetric WO_{3-x} nanoarray. The mirror-symmetric WO_{3-x} nanoarray (MSN-WO_{3-x}) was obtained by a thermal reduction over the WO_3 array at 350 °C for 2 h in the mixed H_2/Ar (10/90) atmosphere.

Preparation of the mirror-symmetric Ru/WO_{3-x} nanoarray. The MSN-WO_{3-x} array (1 cm × 1.5 cm) was immersed in 2 ml 2.0 mg/mL $RuCl_3$ solution for 30 min. Subsequently, the MSN-WO_{3-x} was taken out and dried in an infrared desiccator for 8 min to obtain $RuCl_3$/MSN-WO_{3-x}. Finally, the Ru/MSN-WO_{3-x} array was obtained by a thermal reduction over $RuCl_3$/WO_{3-x} at 250 °C for 2 h in H_2/Ar (10/90) atmosphere.

Electrochemical measurements. The electrochemical performances of samples in the three-electrode system were assessed using an H-type cell separated by a Nafion 117 membrane (DuPont). The Nafion membrane requires pretreatment before being used for electrochemical testing. It was boiled in 3% H_2O_2 for one hour, then boiled in deionized H_2O for two hours, and finally boiled in 0.5 M H_2SO_4 for one hour. After that, it was rinsed with deionized H_2O and kept in deionized H_2O on standby. All electrochemical measurements were performed by employing a CHI Electrochemical Workstation (Model 760E) in a three-electrode system. In typical testing, the NF with the catalysts (active surface kept at 1×1 cm^2) and Ag/AgCl (in saturated KCl solution) are used as the working electrode and reference electrode, respectively, both of which were placed in the cathodic chamber. Meanwhile, Pt mesh was put in an anodic chamber as the counter

electrode. For the NO_3RR process, the cathodic cell was bubbled with ultra-pure Argon (99.999%) for 15 min before the electrolytic process. 0.1 M KNO_3/0.25 M K_2SO_4 solution buffered with 0.5 M phosphate (pH = 7) was adopted as the nitrate reduction electrolyte. Linear sweep voltammetry (LSV) was recorded at a scan rate of 2 mV/s for the NO_3RR process. Electrochemical impedance spectroscopy (EIS) measurements were performed in the range from 100 kHz to 0.01 Hz with a perturbation of 5 mV amplitude. To estimate the C_{dl}, cyclic voltammetry (CV) was carried out in the non-Faradaic potential region from 0.6 to 0.8 V *vs*. RHE with various scan rates, and then the capacitive current $\Delta j = (j_a - j_c)/2$ at 0.7 V was plotted versus the scan rate. The chronoamperometry curves were tested and maintained for 1 h at different potentials. The calibration of E(Ag/AgCl) to E(RHE) was conducted in H_2-saturated electrolyte by applying cyclic voltammetry (CV) at a scan rate of 1 mV s^{-1} on a pair of Pt wires, which served as the working electrode and counter electrode, respectively. The average of E at which the cathodic current and the anodic current both crossed zero was considered as thermodynamic potential for the hydrogen electrode reactions. And the function of E(RHE) about E(Ag/AgCl) can be expressed as follows: E(RHE) = E(Ag/AgCl) + 0.600 V. It is worth noting that the applied potentials in electrochemical testing were not corrected for *iR* drop and the resistance of the system obtained from three measurements of the electrochemical impedance spectroscopy is 2.90 ± 0.05 Ω.

Determination and quantitation of ammonia using UV−Vis. The NH_3 concentration was spectrophotometrically detected by the indophenol blue method with modification.[1] First, the outlet electrolyte product was collected and diluted to the detection range. Next, 1 mL of the diluted sample was mixed with 1 mL of 1 M KOH, 5 wt% salicylic acid, and 5 wt% sodium citrate solution. Then, 0.5 mL of 0.05 M NaClO solution and 0.1 mL of 1.0 wt% $C_5FeN_6Na_2O$ (sodium nitroferricyanide) solution was added and left to rest for 2 h under ambient conditions. The absorption spectrum of the resulting solution was recorded via an ultraviolet-visible spectrophotometer at 650 nm. The concentration−absorbance curve was calibrated using a series of standard ammonium chloride solutions at the electrolyte, and the ammonium chloride crystal was dried at 105 °C for 2 h in advance.

Determination and quantitation of ammonia using ^{1}H NMR. In addition,^{1}H NMR spectroscopy (500 MHz) was also used to detect ammonia in the isotope-labelling measurement. The collected NH_3 sample was first diluted to the detection range and adjusted to pH 2.0 by adding 0.1 M HCl. Next, 0.5 ml of the sample solution was mixed with 0.1 ml DMSO-d_6 (dimethyl sulfoxide-d6) and 0.04 wt% $C_4H_4O_4$, where DMSO-d_6 serves as a solvent and maleic acid ($C_4H_4O_4$) as the internal standard. Finally, the prepared mixture was tested by a 500 MHz SB Liquid Bruker Avance NMR spectrometer at ambient conditions and the NH_3 product peaks were analyzed.

Determination and quantitation of nitrite using UV-Vis. The concentration of nitrite in the electrolyte was estimated by Griess reagent.[2] Griess reagent was prepared by a mixture of 0.1 g N-(1-naphthalene) ethyldiamine dihydrochloride, 1.0 g sulfanilamide, and 2.94 mL H_3PO_4 dissolved in 50 mL DI water. First, the outlet electrolyte product was collected and diluted to the detection range. Next, 1 mL of the diluted sample was mixed with 2 mL DI water and 1 mL Griess reagent in sequence. After 10 min, the absorption spectrum of the resulting solution was recorded via an ultraviolet-visible spectrophotometer at 540 nm. The

concentration−absorbance curve was calibrated using a series of standard potassium nitrite solutions at the electrolyte, and the potassium nitrite crystal was dried at 105 °C for 2 h in advance.

Characterization. XRD patterns of the products were tested with an X-ray diffractometer (Tongda TD–3500) by Cu Kα radiation. The morphologies and element composition were sequentially investigated by a field-emission SEM (FESEM, S4800, Hitachi, Japan), energy-dispersive X-ray spectroscope (EDX, GENESIS, EDAX, USA), and transmission electron microscope (TEM, Tecnai G220, Fei Corporation, Japan). The chemical states of the samples were analyzed with X-ray photoelectron spectroscopy (XPS, Thermo ESCALAB 250Xi, Thermoelectricity Instruments, USA) surface analysis system. EPR experiment was conducted on a Bruker ELEXSYS E500. The component content was investigated via inductively coupled plasma optical emission spectroscopy (ICP-OES, Agilent, USA). The isotope-labeled samples were analyzed using a 500-MHz ^{1}H-NMR spectrometer (Bruker). ^{1}H MAS NMR experiments were performed using a 600-MHz spectrometer (Bruker, probe: 4 mm, spinning rate: 12 kHz). UV-Vis absorption spectra were taken using a UV-Vis spectrophotometer (YIPU, U-T3C). Raman spectra were recorded on a LabRAM HR800 Raman spectrometer (HORIBA Jobin Yvon) using 532 nm laser with 10% laser power. The differential electrochemical mass spectrometry (DEMS, QAS 100) was provided by Linglu instruments (Shanghai) Co. Ltd. The infrared absorption spectra were recorded on a Thermo Nicolet 8700 spectrometer equipped with MCT detector cooled by liquid nitrogen.

Electrochemical in situ Raman tests. The surface enhanced Raman spectroscopy (SERS) was employed to detect the surface alteration of the catalysts during NO_3RR. The in-situ electrolytic cell used was provided by Gaossunion. We used an electrochemically roughened gold (Au) as a substrate to obtain the surface-enhanced effect. First, the Au was mechanically polished with alumina powder (500 nm) and then sonicated several times in 1:1 mixture of ethanol and acetone and then in ultrapure water. The clean Au was subjected to 20 oxidation-reduction cycling between -0.28 and 1.22 V vs. Ag/AgCl in 0.1 M KCl solution, in which the potential was held for 10 s at the negative limit and 5 s at the positive limit. After the potential cycling, the Au surface was reduced for 5 min at a constant potential of -0.3 V. Finally, the resulting brownish Au surface was thoroughly rinsed with ultrapure water.[3] We detached MSN-WO_{3-x} and Ru/MSN-WO_{3-x} from the NF substrate through ultrasonic treatment and then dropped them onto an Au electrode for in situ SERS measurements. The specific process is as follows:5.0 mg of the catalysts was added to 480 μL of anhydrous ethanol and 20 μL of Nafion solution (5 wt.%), and then ultrasonically dispersed for 30 minutes to obtain the catalyst ink. Dropping ink onto the pretreated gold electrode, we controlled the catalyst mass loading to 2 mg cm^{-2}. To avoid the interference of carbon bands in Ru/C, Ru is electrodeposited on Au substrate directly via a potential-cycling method. In detail, 1 M PBS (50 mL) containing 2 mg/mL $RuCl_3$ was taken as the electrodeposition solution. Then, the electrochemically roughened Au was subjected to 100 cycles of reduction at a scan rate of 50 mV s^{-1} between -0.6 and -1.0 V vs Ag/AgCl in the above electrolyte solution.

Electrochemical online DEMS test. The working electrodes were prepared by sputtering Au onto 50 μm thick porous PTFE films. The detached Ru/MSN-WO_{3-x} catalyst was dropped and cast onto the Au film with a mass loading of 2 mg cm^{-2}. Then, the applied voltage (−0.5 V vs. RHE) was employed alternately, and the interval was 200 seconds. After the electrochemical test was over and the mass signal returned to baseline,

the next cycle started using the same conditions to avoid accidental error. After six cycles, the experiment ended.

Electrochemical in situ ATR-FTIR tests. The surface enhanced infrared absorption spectroscopy (SEIRAS) with the attenuated total reflection (ATR) configuration was employed. Electrochemical in situ ATR-FTIR measurements were performed on an electrolytic cell (Gaossunion) mounted on a Pike Veemax III ATR with a single bounce silicon crystal covered with an Au membrane in internal reflection mode. The single-bounce silicon crystal covered with an Au membrane was prepared by the following procedure. (1) NaOH (0.12 g), $NaAuCl_4 \cdot 2H_2O$ (0.23 g), NH_4Cl (0.13 g), Na_2SO_3 (0.95 g) and $Na_2S_2O_3 \cdot 5H_2O$ (0.62 g) were dissolved in H_2O (100 ml) (solution A). (2) Monocrystal silicon was immersed in aqua regia ($V_{concentrated\ HCl}$:V_{HNO3} = 1:1) for 20 min and then polished using alumina powder. After washing three times with water and acetone, clean monocrystal silicon was obtained. (3) The above monocrystal silicon was immersed in a mixture of H_2SO_4 and H_2O_2 ($V_{concentrated\ H2SO4}$:V_{H2O2} = 1:1) for 20 min. (4) After washing three times with water, the above monocrystal silicon was then immersed in 40% NH_4F aqueous solution and washed three times with water. (5) The monocrystal silicon was immersed in a mixture of 15 ml of solution A and 3.4 ml of 2% NH_4F aqueous solution. (6) After 5 min, Au-coated monocrystal silicon was obtained.[4] The detached Ru/MSN-WO_{3-x} catalyst was dropped and cast onto the Au-coated monocrystal silicon with a mass loading of 2 mg cm^{-2}.

Computational methods. Density functional theory (DFT) calculations were performed with the Vienna Ab Initio Simulation Package (VASP).[5] The exchange correlation energy was described by the Perdew–Burke–Ernzenhof (PBE) in the generalized gradient approximation (GGA).[6] The projector augmented wave (PAW) method was used to describe ion-electron interactions.[7] Van der Waals interactions (vdW) were considered by the DFT-D3 method.[8] A cutoff energy of 450 eV for the plane wave basis set was chosen. The convergence criteria for energy and force were set to be 1×10^{-4} eV and 0.02 eV $Å^{-1}$, respectively. A Monkhorst-Pack k-point mesh of 2×2×1 was chosen for all models in the optimization of the supercell structure. The Gibbs reaction free energy (ΔG) was calculated based on the computational hydrogen electrode (CHE) model.[9] The ΔG for each step in the NH_3 synthesis process can be evaluated according to the equation below:

$$\Delta G = \Delta E + \Delta E_{ZPE} - T\Delta S$$

in which ΔE is the change of the total energy between the products and reactants; ΔE_{ZPE} and ΔS indicate the differences in the zero-point energy and entropy before and after adsorption. T is temperature, which is set to 298.15K.

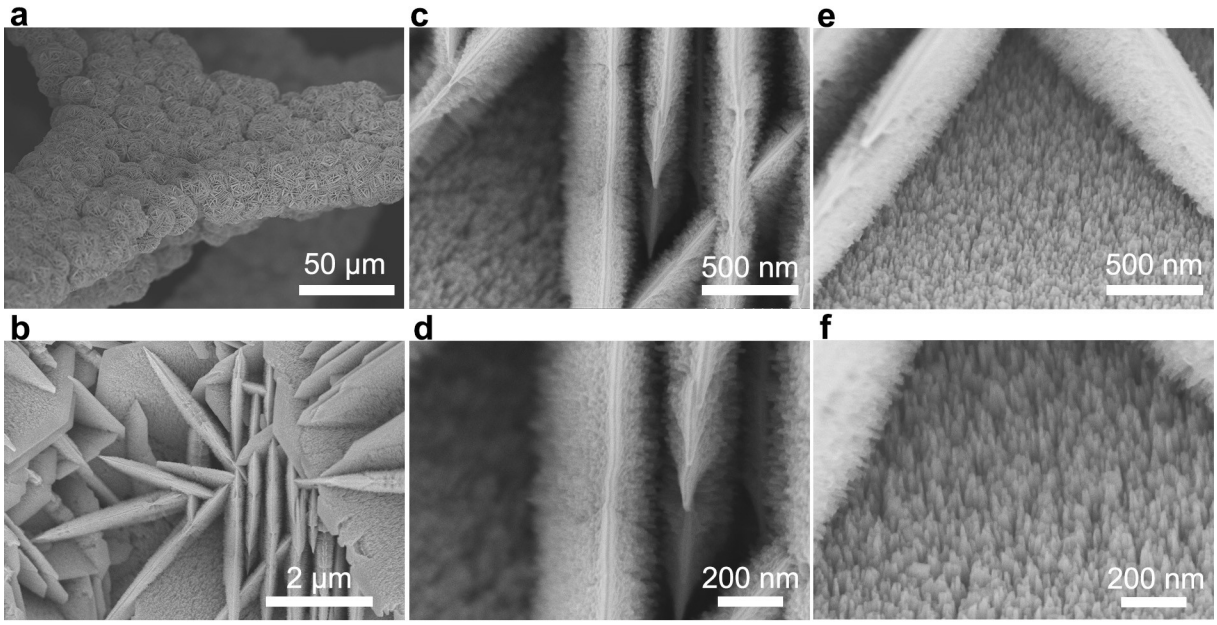

Fig. S1 (a-f) SEM images of the WO_3 nanoarray synthesized with the AMT amount of 0.2 mmol. Mass loading: 18.6 mg cm^{-2}.

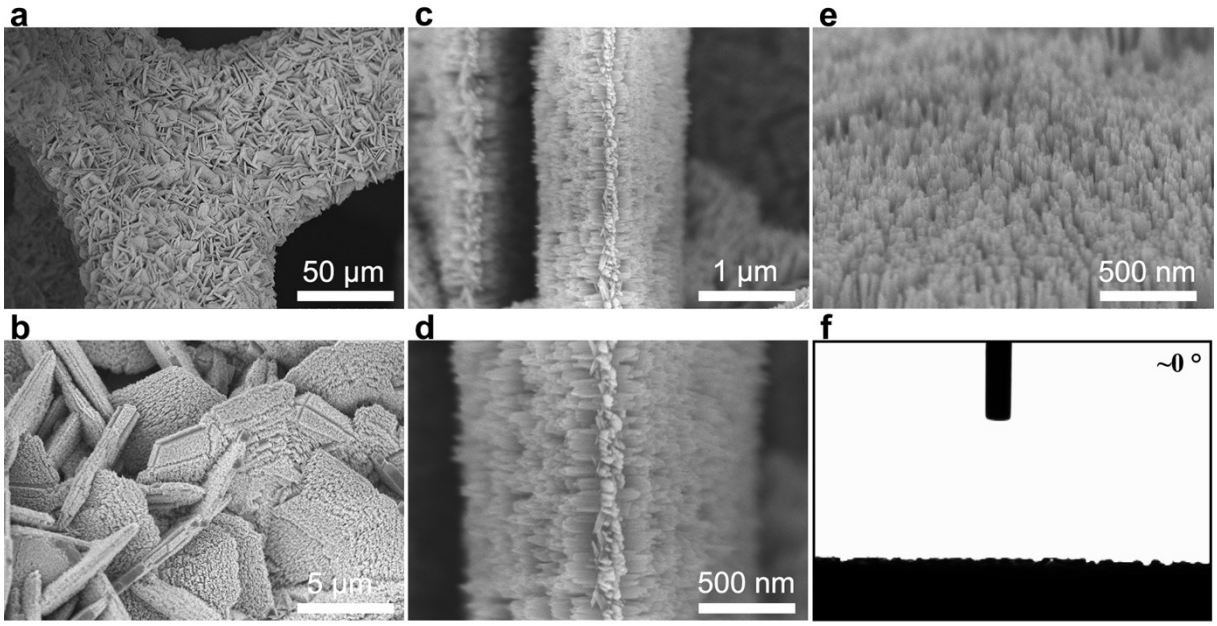

Fig. S2 (a-e) SEM and (f) contact angle images of the WO_3 nanoarray synthesized with the AMT amount of 0.4 mmol. Mass loading: 27.4 mg cm^{-2}.

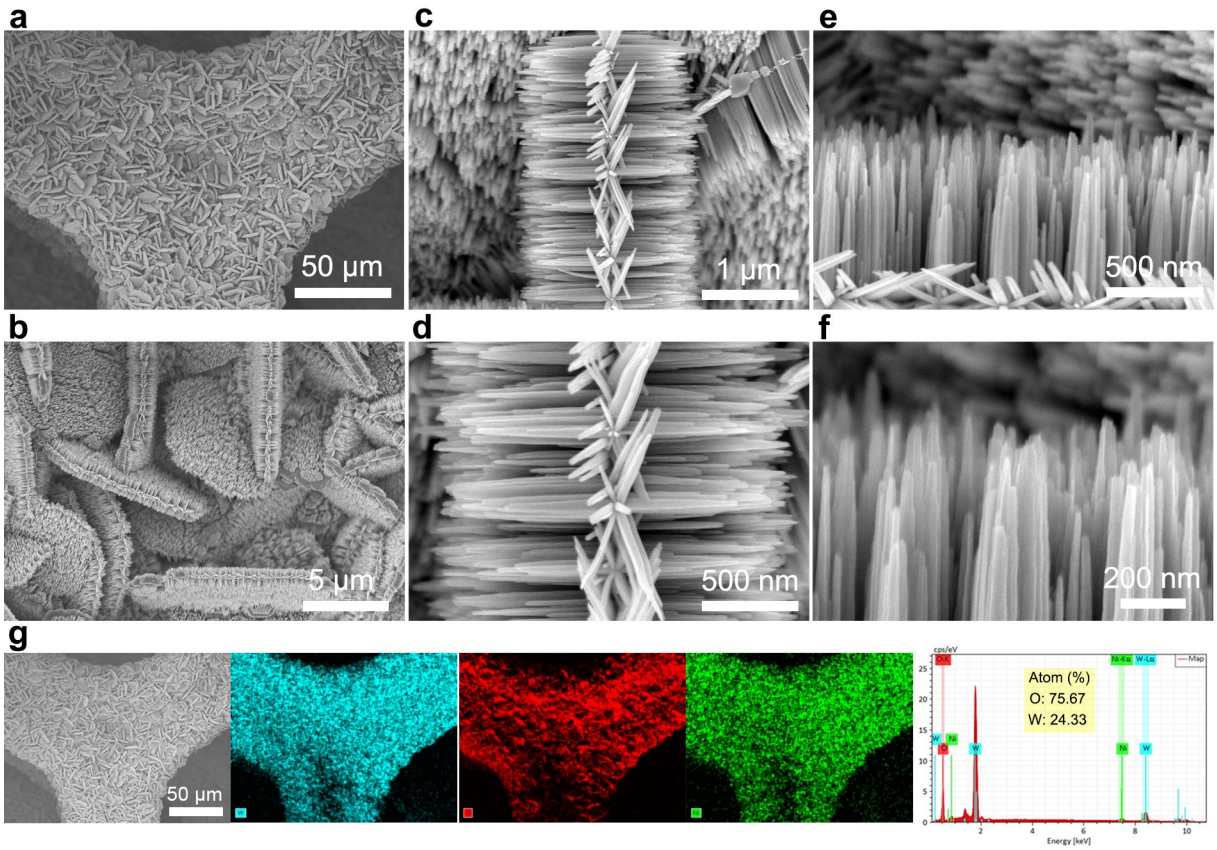

Fig. S3 (a-f) SEM and (g) SEM-EDS mapping images of the MSN-WO_3 synthesized with the AMT amount of 0.6 mmol. Mass loading: 41.3 mg cm^{-2}.

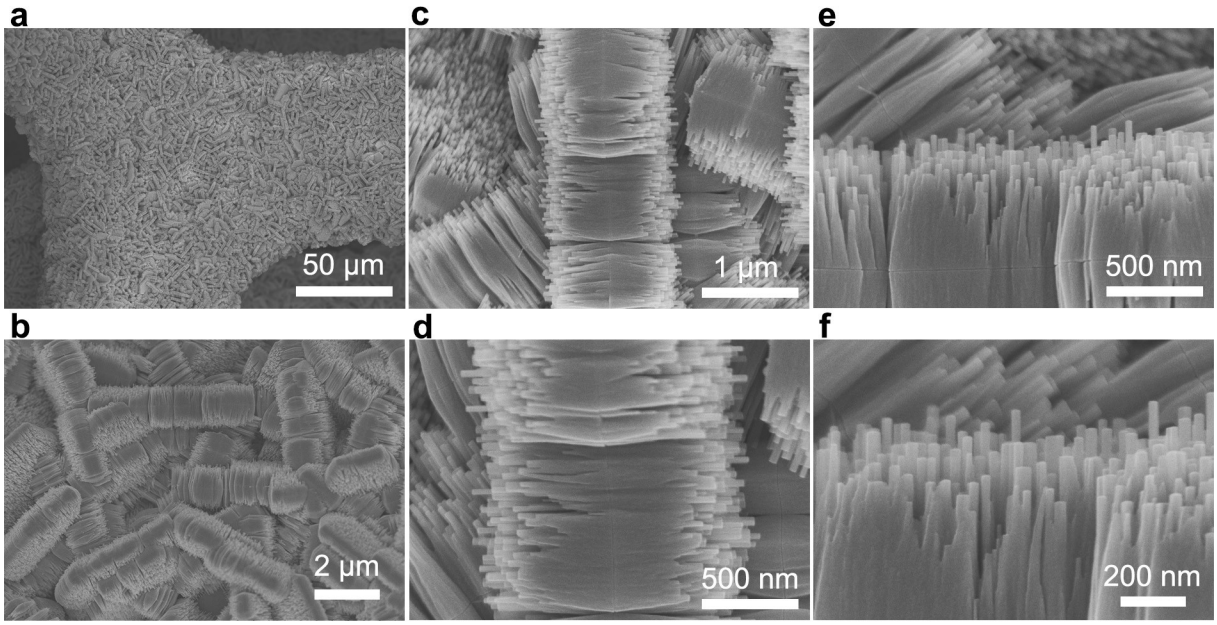

Fig. S4 (a-f) SEM images of the WO_3 nanoarray synthesized with the AMT amount of 0.8 mmol. Mass loading: 49.7 mg cm^{-2}. In this case, such a high tungsten source amount results in the excessive lateral growth of WO_3 nanorods.

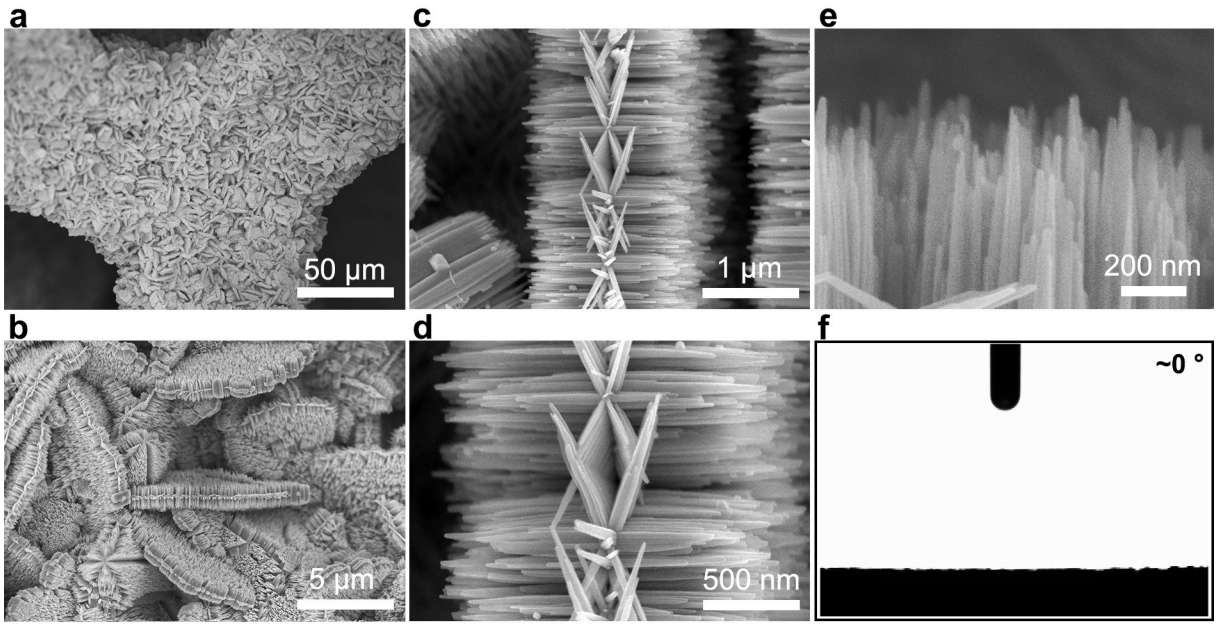

Fig. S5 (a-e) SEM and (f) contact angle images of MSN-WO_{3-x}.

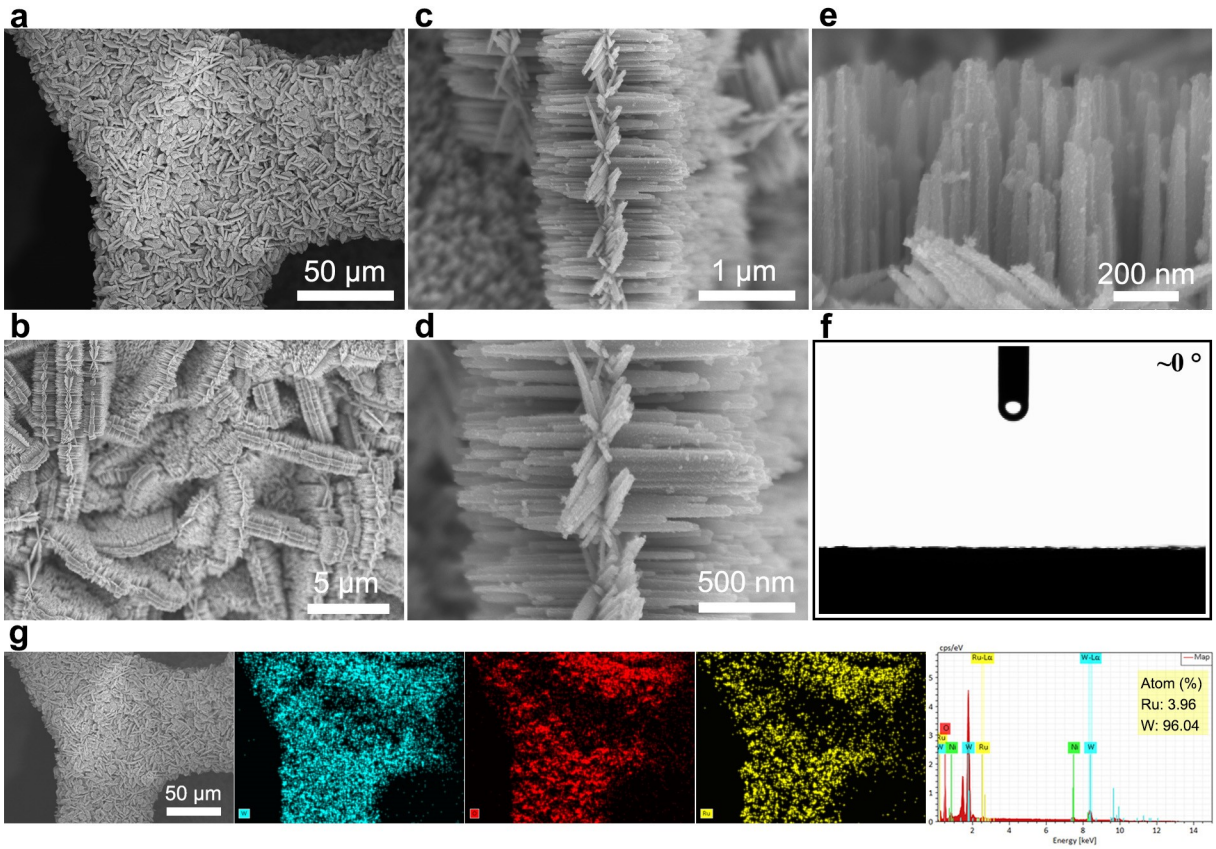

Fig. S6 (a-e) SEM, (f) contact angle, and (g) SEM-EDS mapping of Ru/MSN-WO_{3-x}.

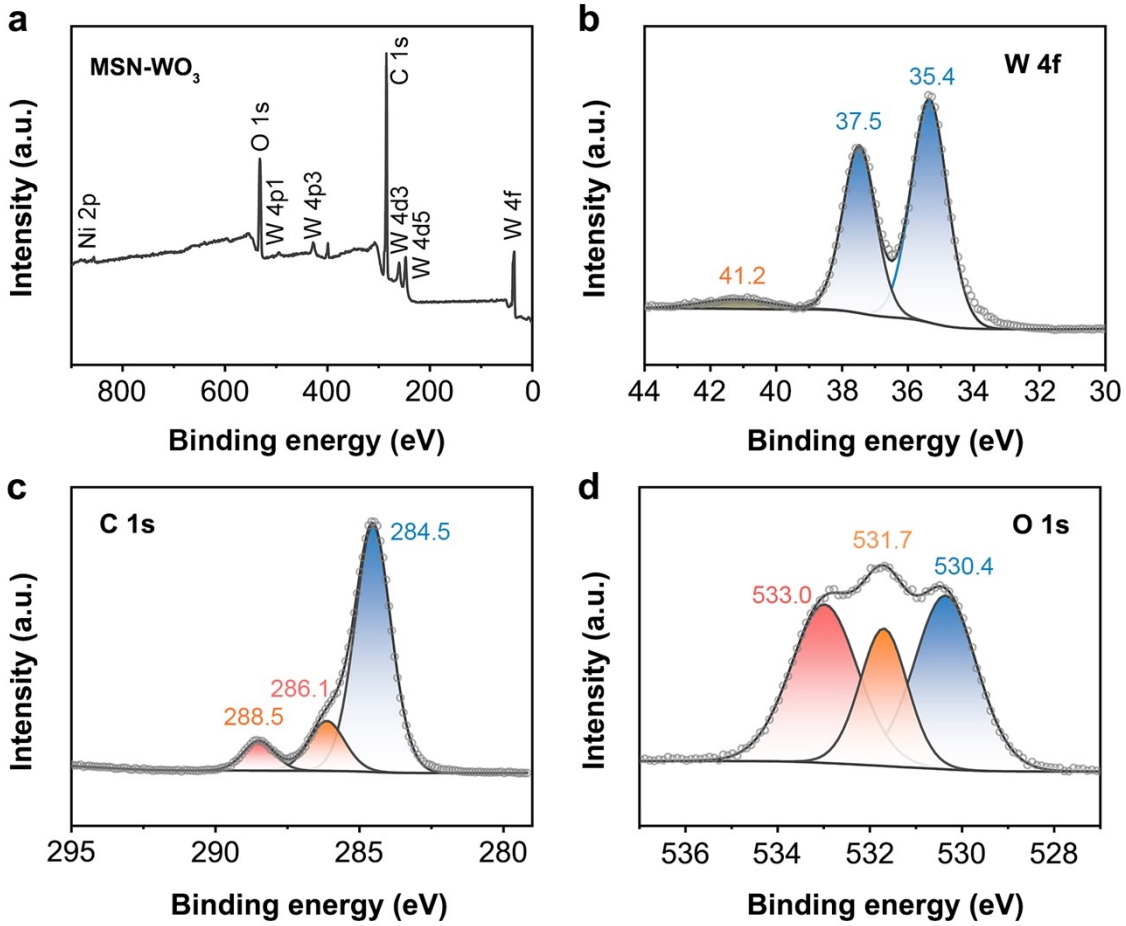

Fig. S7 (a) XPS survey spectra, high resolution (b) W 4f, (c) C 1s, and (d) O 1s XPS spectra of MSN-WO_3.

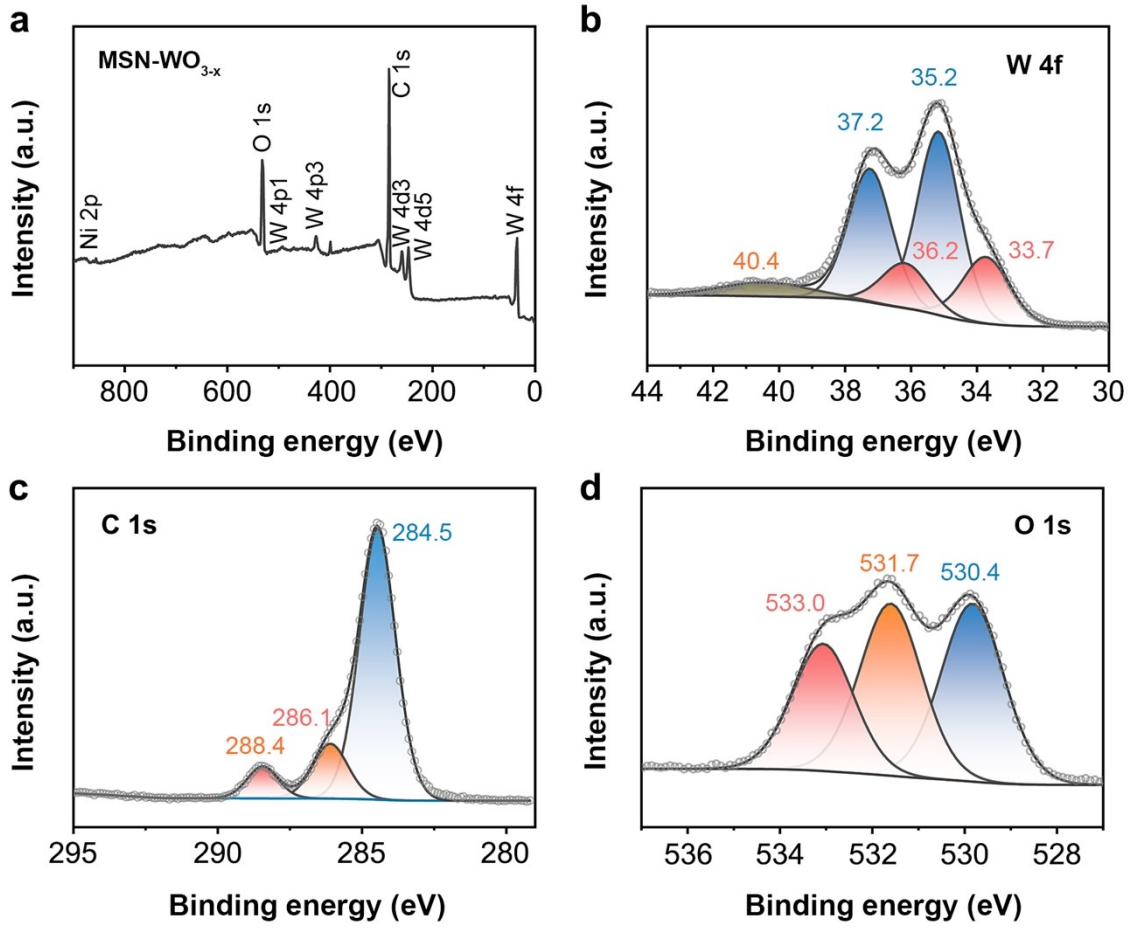

Fig. S8 (a) XPS survey spectra, high resolution (b) W 4f, (c) C 1s, and (d) O 1s XPS spectra of MSN-WO_{3-x}.

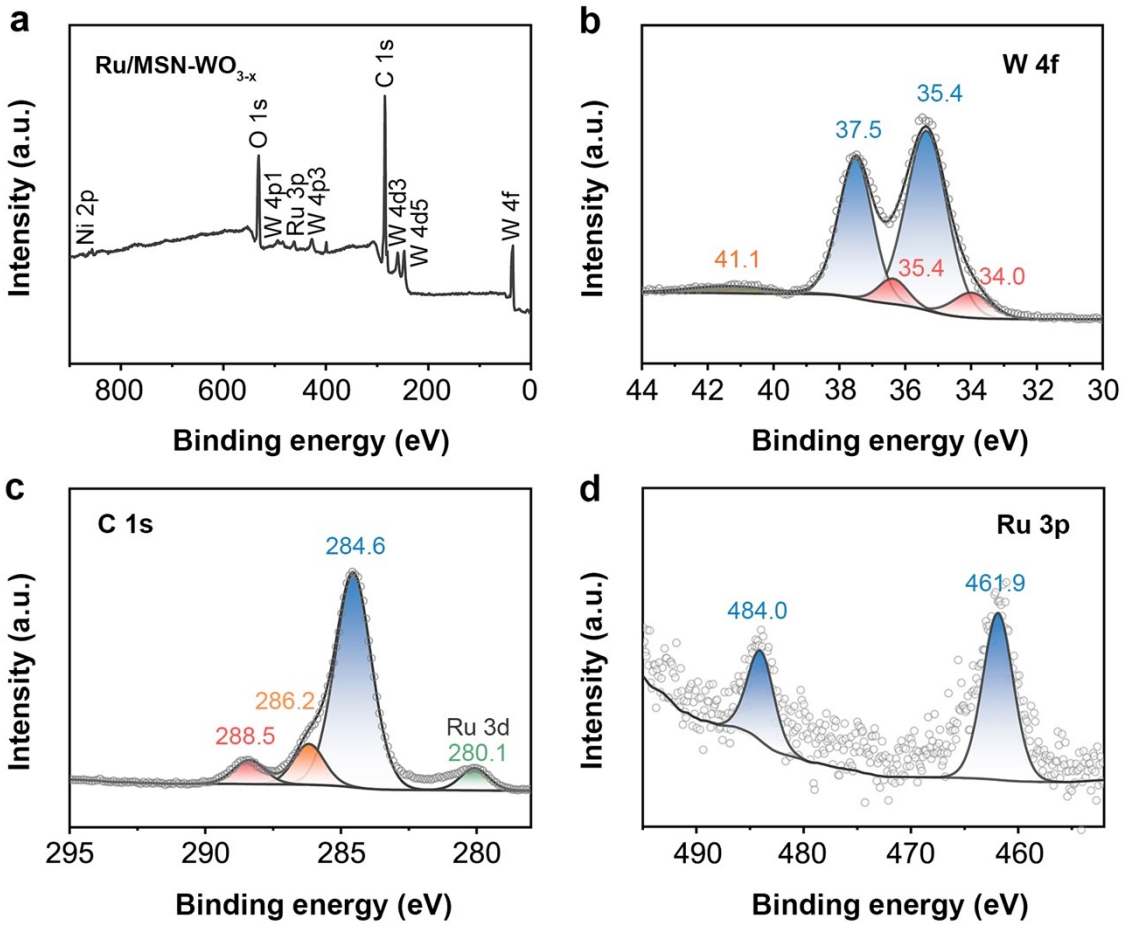

Fig. S9 (a) XPS survey spectra, high resolution (b) W 4f, (c) C 1s, and (d) Ru 3p XPS spectra of Ru/MSN-WO_{3-x}.

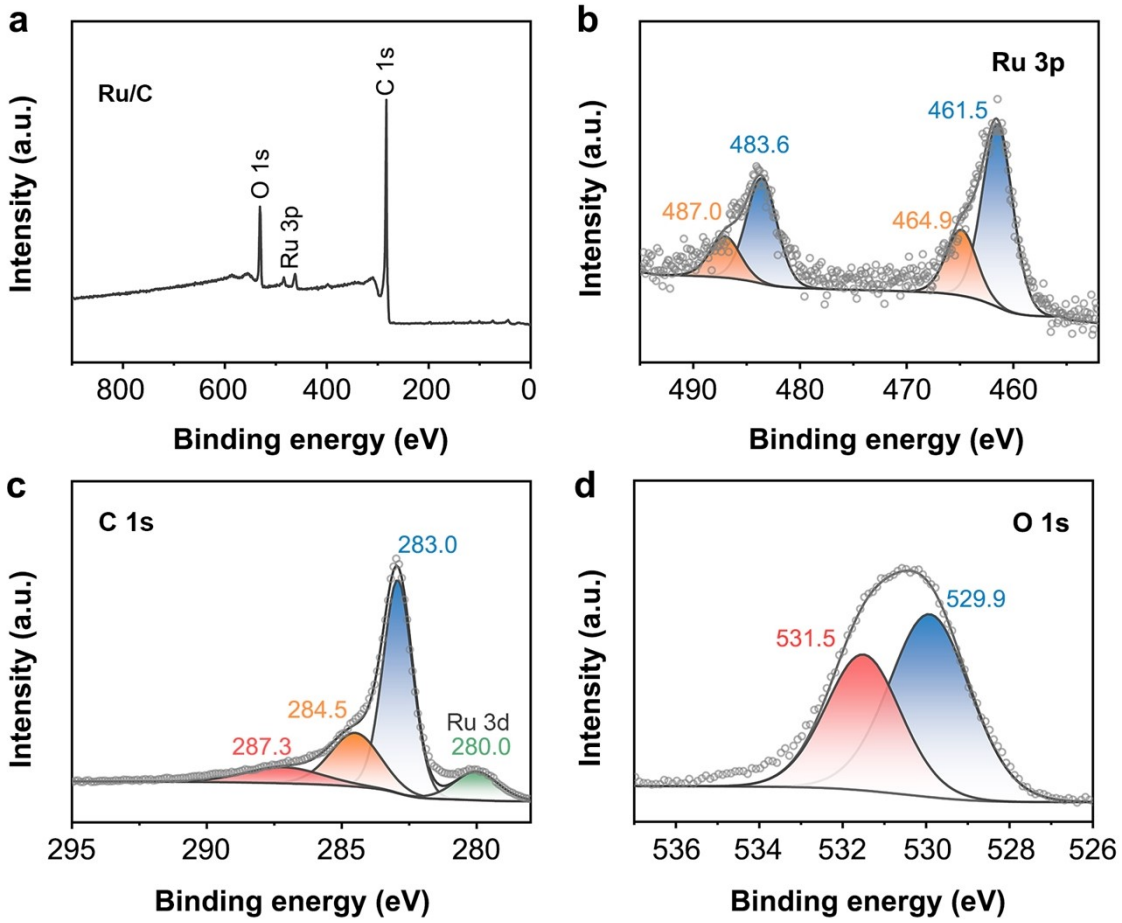

Fig. S10 (a) XPS survey spectra, high resolution (b) Ru 3p, (c) C 1s, and (d) O 1s XPS spectra of Ru/C.

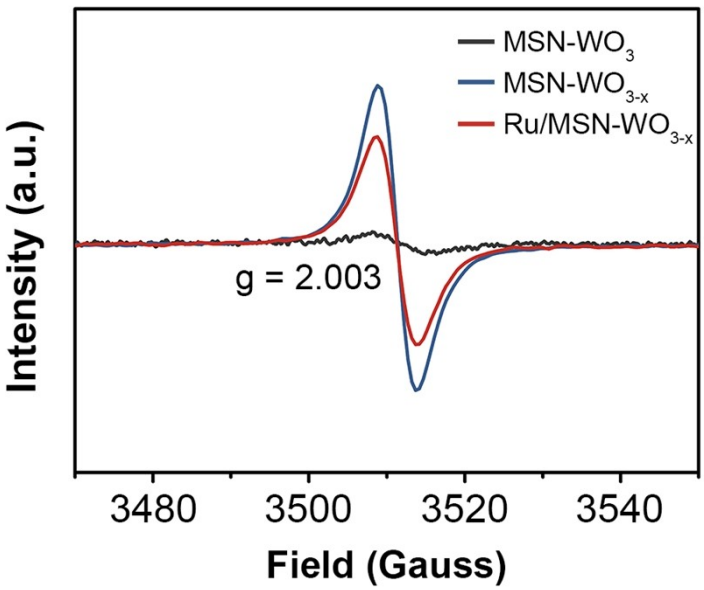

Fig. S11 EPR spectra of MSN-WO_3, MSN-WO_{3-x}, and Ru/MSN-WO_{3-x}.

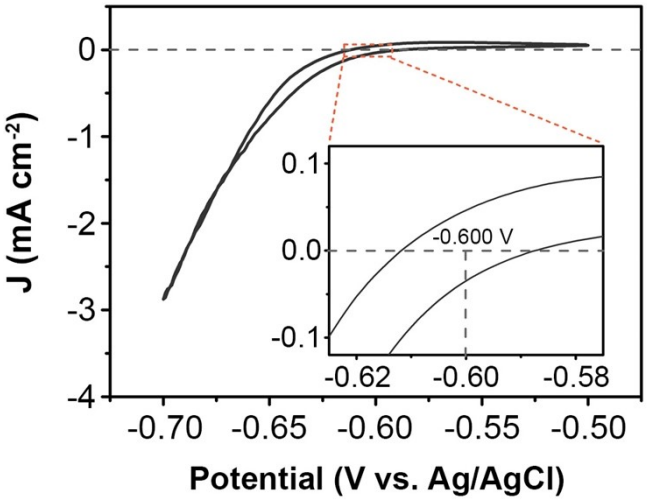

Fig. S12 The calibration result of Ag/AgCl reference electrode to RHE in a neutral electrolyte. The CV tests are carried out after pumping high-purity hydrogen for 30 min to saturate the electrolyte.

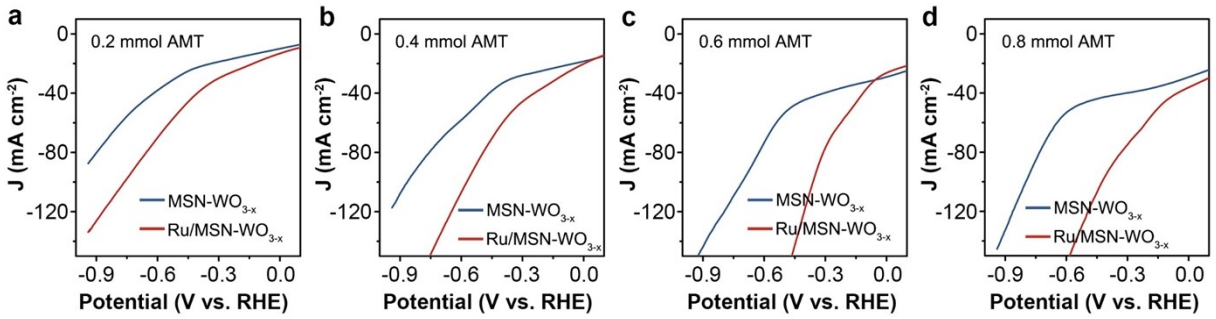

Fig. S13 LSV curves of Ru/MSN-WO_{3-x} synthesized with (a) 0.2 mmol AMT, (b) 0.4 mmol AMT, (c) 0.6 mmol AMT, and (d) 0.8 mmol AMT.

Hereinto, Ru/MSN-WO_{3-x} synthesized with 0.6 mmol AMT shows the largest current response since the moderate lateral growth of tungsten oxide could offer abundant exposed sites for loading Ru clusters.

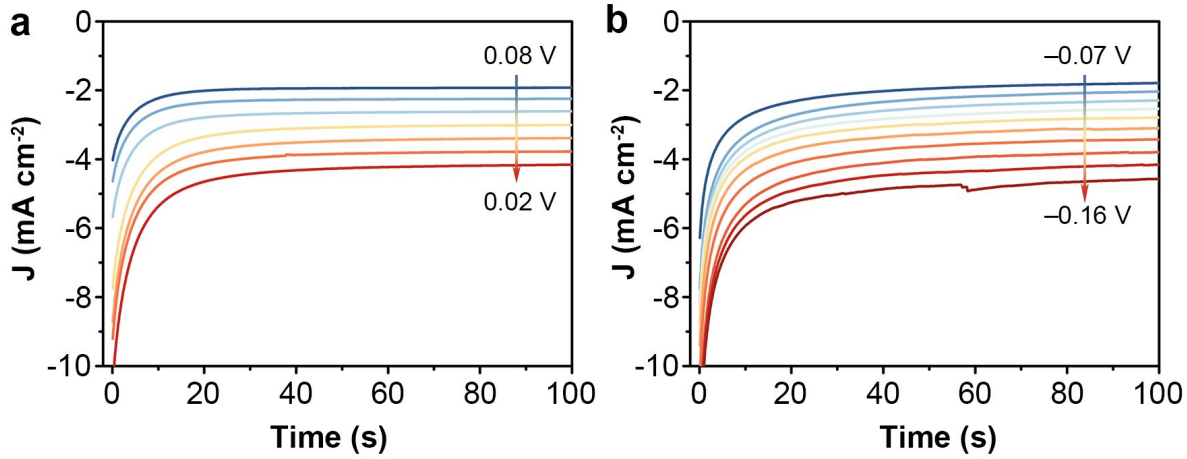

Fig. S14 Chronoamperometry tests over (a) Ru/MSN-WO_{3-x} and (b) MSN-WO_{3-x} by stepping the potential at 10-mV intervals for evaluating the steady state current response and Tafel slope.

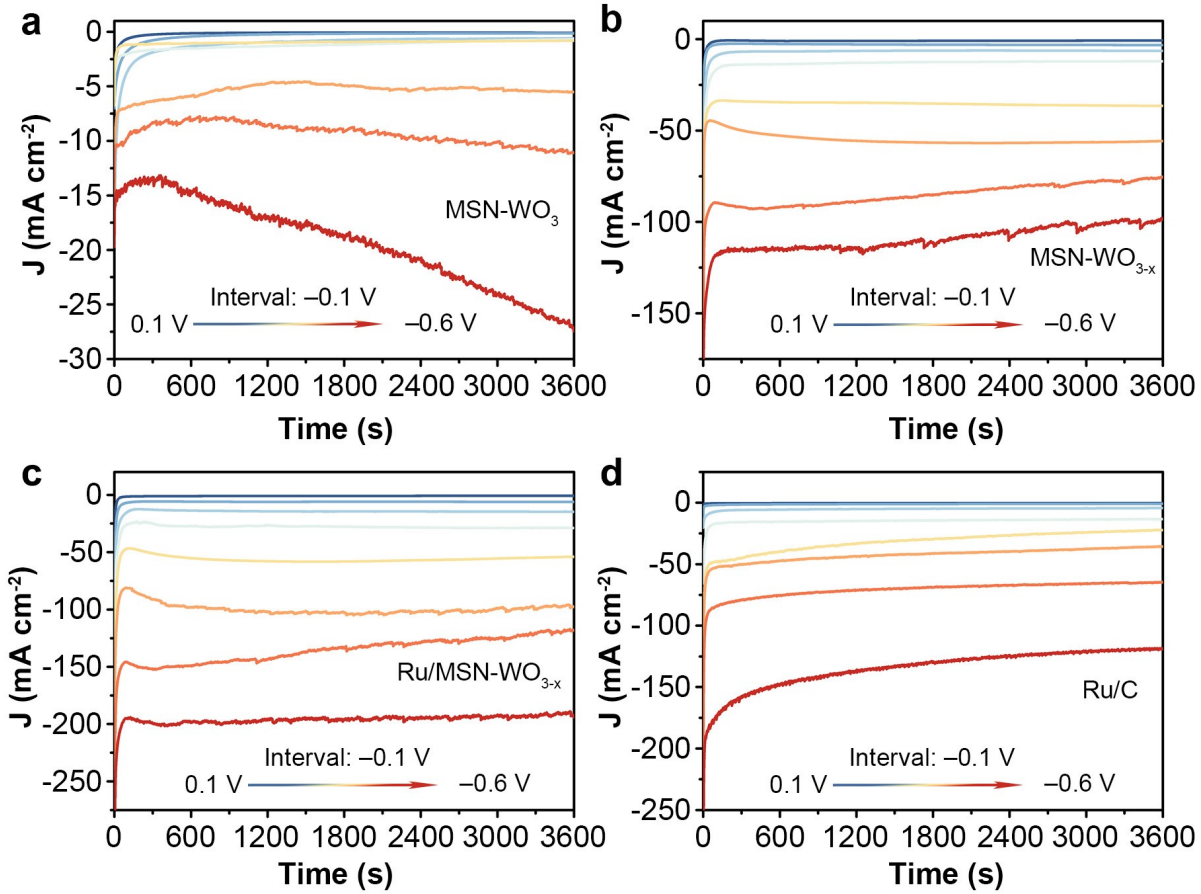

Fig. S15 The current density curves of chronoamperometry measurement at different potentials (vs. RHE) over (a) MSN-WO_3, (b) MSN-WO_{3-x}, (c) Ru/MSN-WO_{3-x}, and (d) Ru/C.

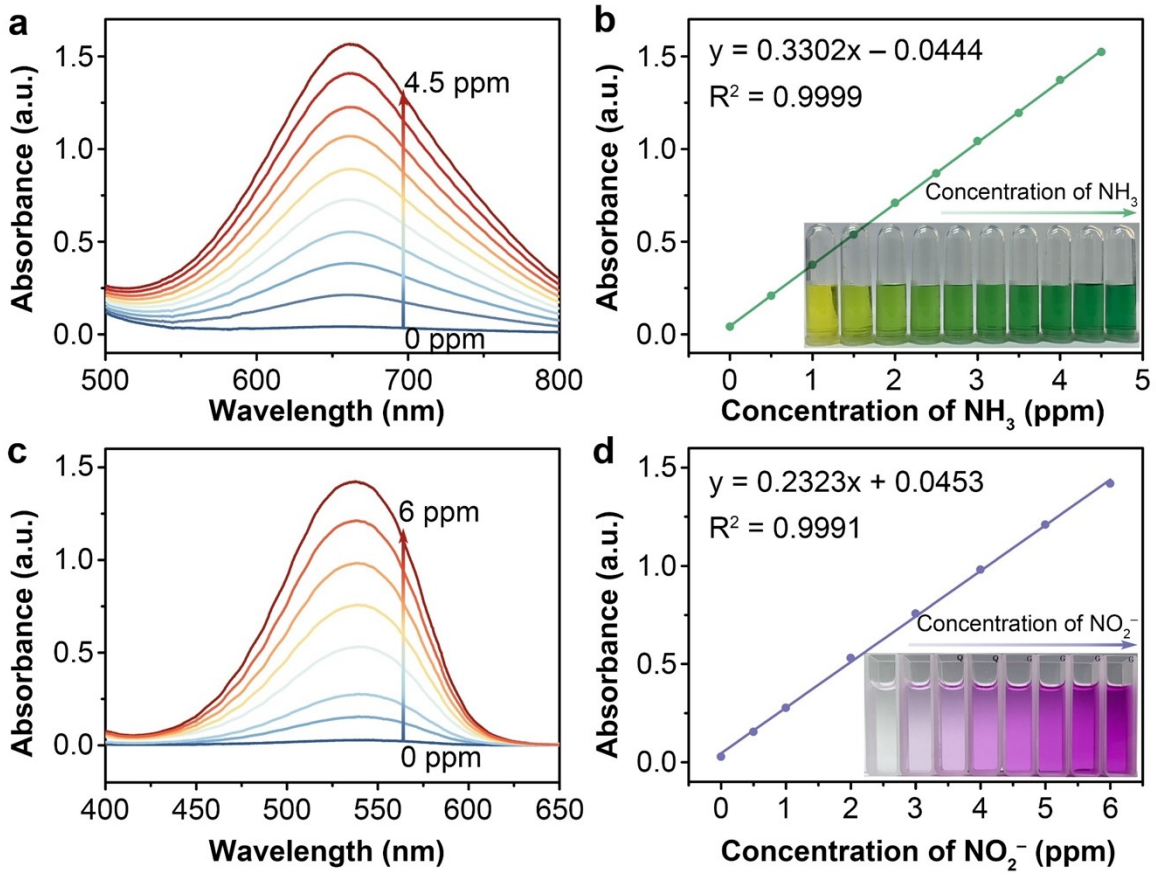

Fig. S16 (a) UV-Vis curves of electrolyte solution with different NH_3 concentrations after 2 h coloration of the indophenol assays. (b) Linear fitting of the corresponding calibration curve for the relationship between the absorbance and NH_3 concentration; Insert: Photograph of solution colored by the indophenol indicator with increasing NH_3 concentration. (c) UV-Vis spectroscopy curves of electrolyte solution with different nitrite concentrations after 10 min coloration of the Griess reagent. (d) Linear fitting of the corresponding calibration curve for the relationship between the absorbance and nitrite concentration; Insert: Photograph of solution with the increasing NO_2^- concentration colored by the Griess reagent.

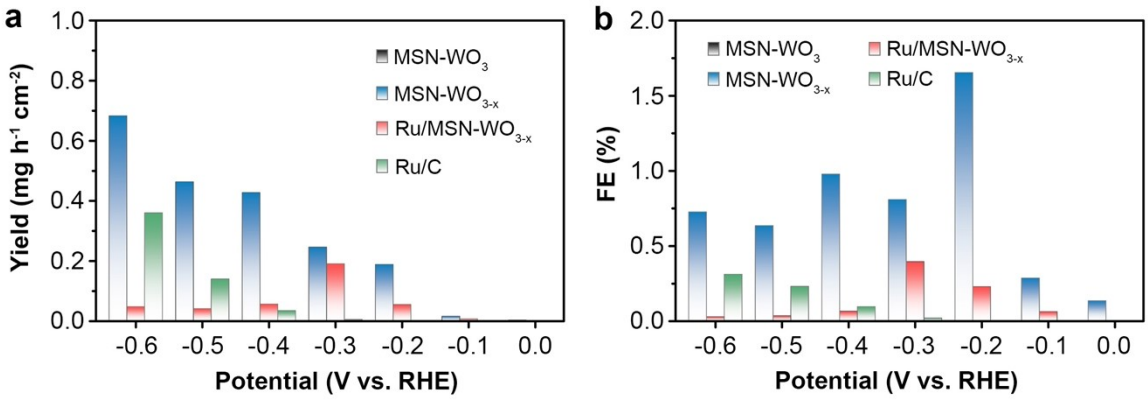

Fig. S17 (a) NO_2^- yield rate and (b) FE over MSN-WO_3, MSN-WO_{3-x}, Ru/MSN-WO_{3-x}, and Ru/C at various potentials.

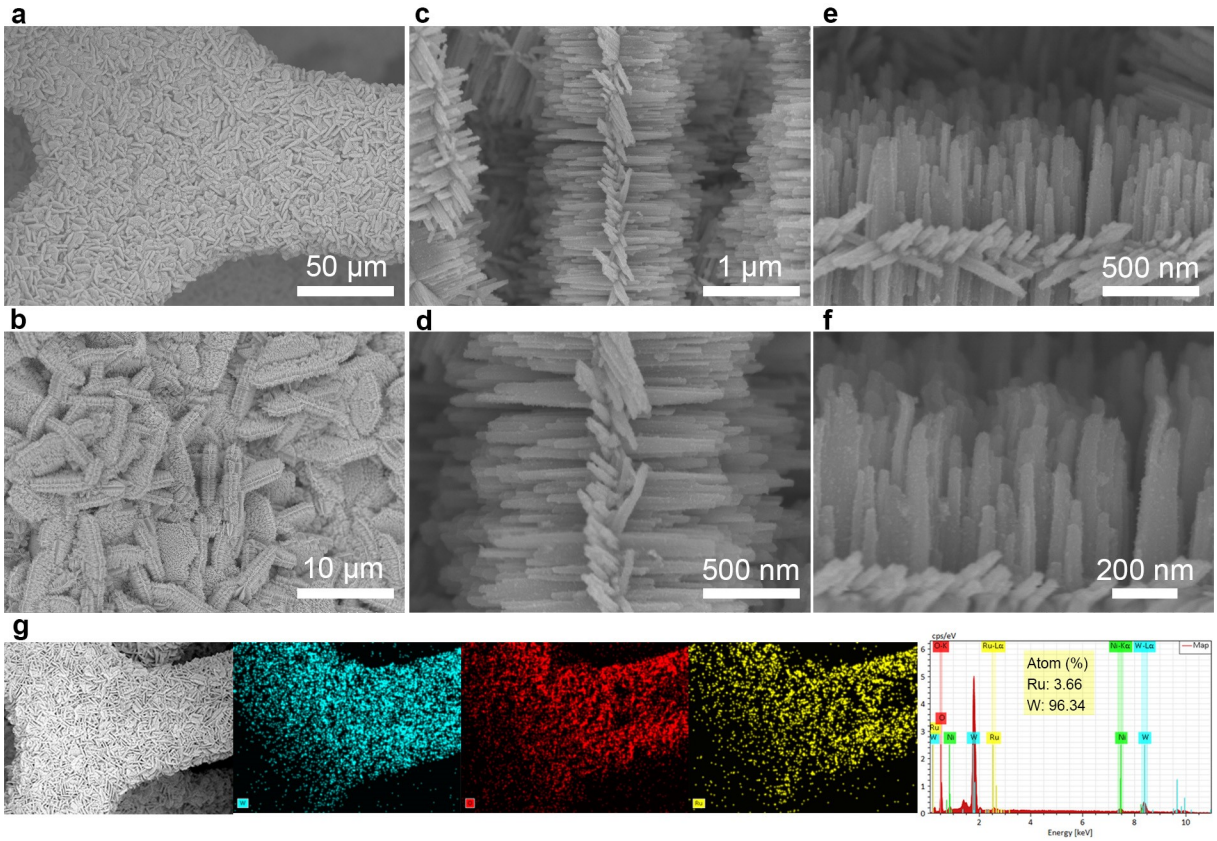

Fig. S18 (a-f) SEM images and (g) the corresponding mapping images of the Ru/MSN-WO_{3-x} after NO_3RR.

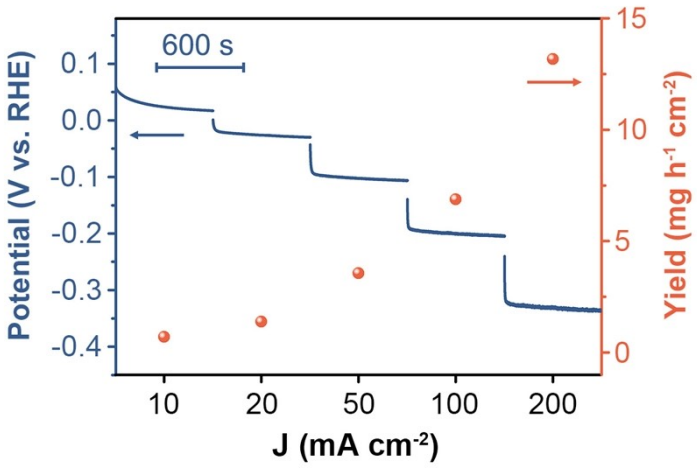

Fig. S19 Chronopotentiometry curves and ammonia yield rates of NO_3RR over Ru/MSN-WO_{3-x} at different current densities with a magnetic stirring rate of 600 rpm.

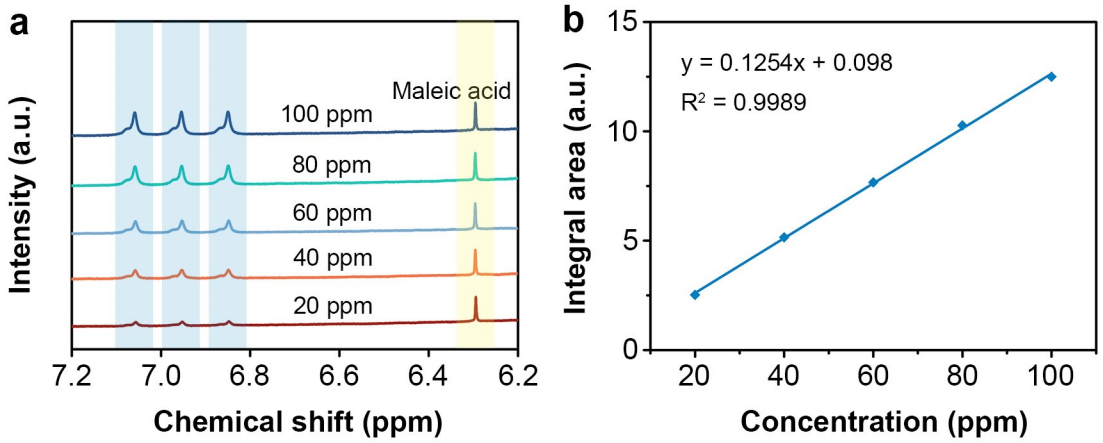

Fig. S20 (a) ^{1}H NMR of ammonia-^{14}N with different concentrations and (b) the corresponding standard curve. The concentration of ammonia-^{14}N can be quantitatively determined by ^{1}H NMR with external standards (maleic acid). The proton signal of maleic acid appears at δ = 6.29 ppm. The ^{1}H NMR spectra of $^{14}NH_4^+$ show triple peaks at δ = 6.85, 6.95, and 7.06 ppm. The calibration curve shows good linearity.

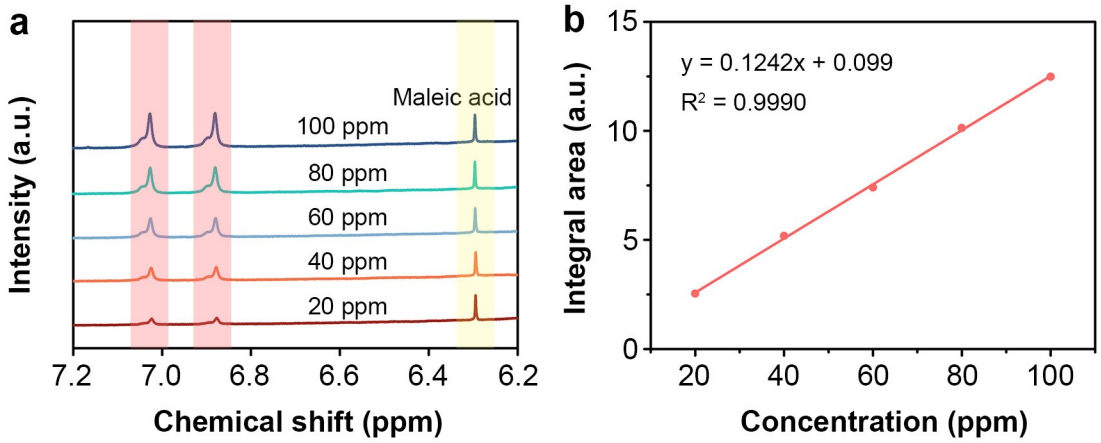

Fig. S21 (a) ^{1}H NMR of ammonia-^{15}N with different concentrations and (b) the corresponding standard curve. The concentration of ammonia-^{15}N can be quantitatively determined by ^{1}H NMR with external standards (maleic acid). The proton signal of maleic acid appears at δ = 6.29 ppm. The ^{1}H NMR spectra of $^{15}NH_4^+$ show double peaks at δ = 6.88 and 7.02 ppm. The calibration curve shows good linearity.

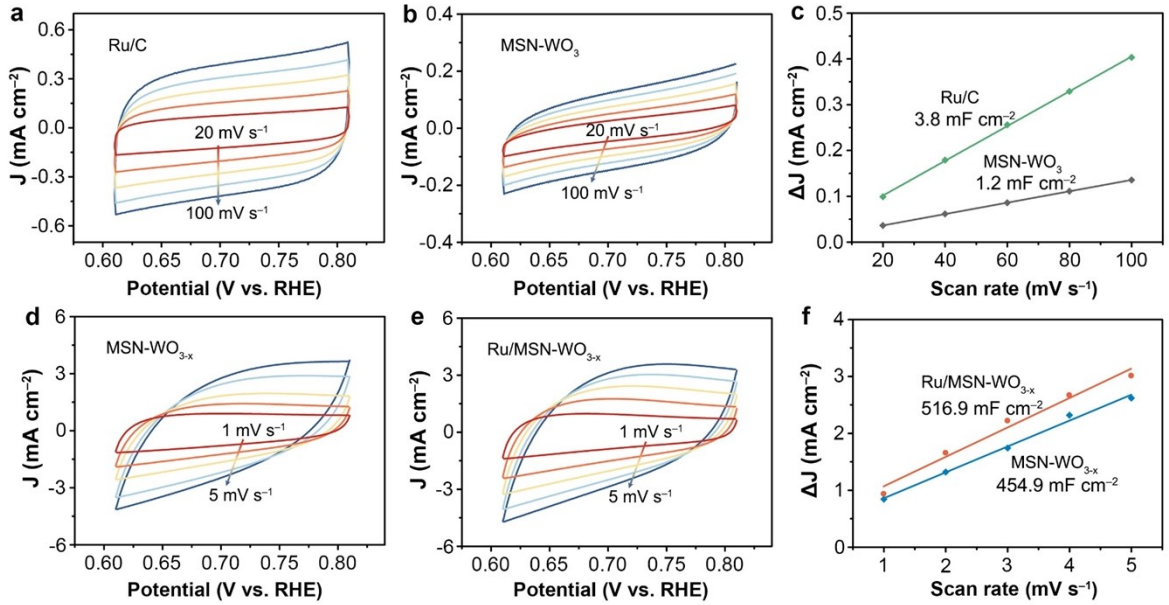

Fig. S22 CV curves and capacitive currents plotted as the function of scan rates for the calculation of double-layer capacitance. (a) CV curves of Ru/C and (b) MSN-WO_3 recorded at various scan rates. (c) The capacitive current measured at 0.7 V (vs. RHE) plotted as a function of scan rate of Ru/C and MSN-WO_3. (d) CV curves of MSN-WO_{3-x} and (e) Ru/MSN-WO_{3-x} recorded at various scan rates. (f) The capacitive current measured at 0.7 V (vs. RHE) plotted as a function of scan rate of MSN-WO_{3-x} and Ru/MSN-WO_{3-x}.

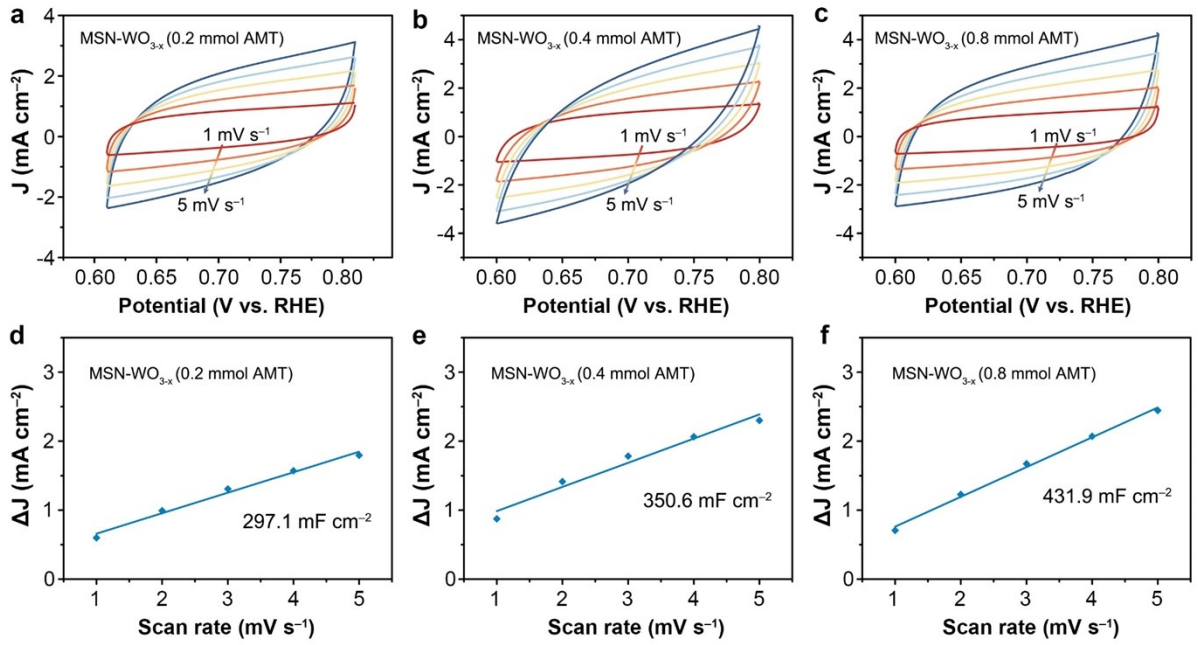

Fig. S23 The comparison of the double-layer capacitance of different MSN-WO_{3-x} supports mentioned above. CV curves of MSN-WO_{3-x} synthesized with (a) 0.2 mmol AMT, (b) 0.4 mmol AMT, and (c) 0.8 mmol AMT. (d-f) The corresponding capacitive current measured at 0.7 V (vs. RHE) plotted as a function of scan rate. Herein, we select the MSN-WO_{3-x} synthesized with 0.6 mmol AMT (Fig. S23d) as the support since it shows the largest C_{dl} value of 454.9 mF cm^{-2}.

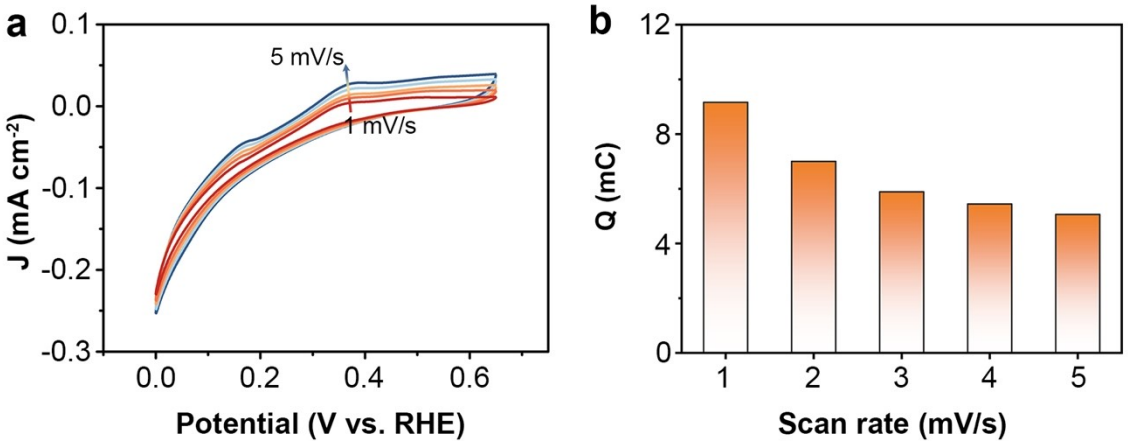

Fig. S24 Capacitance analysis of MSN-WO_3. (a) CV curves recorded at various scan rates. Scan rates vary from 1 to 5 mV/s. (b) Total charge at various scan rates.

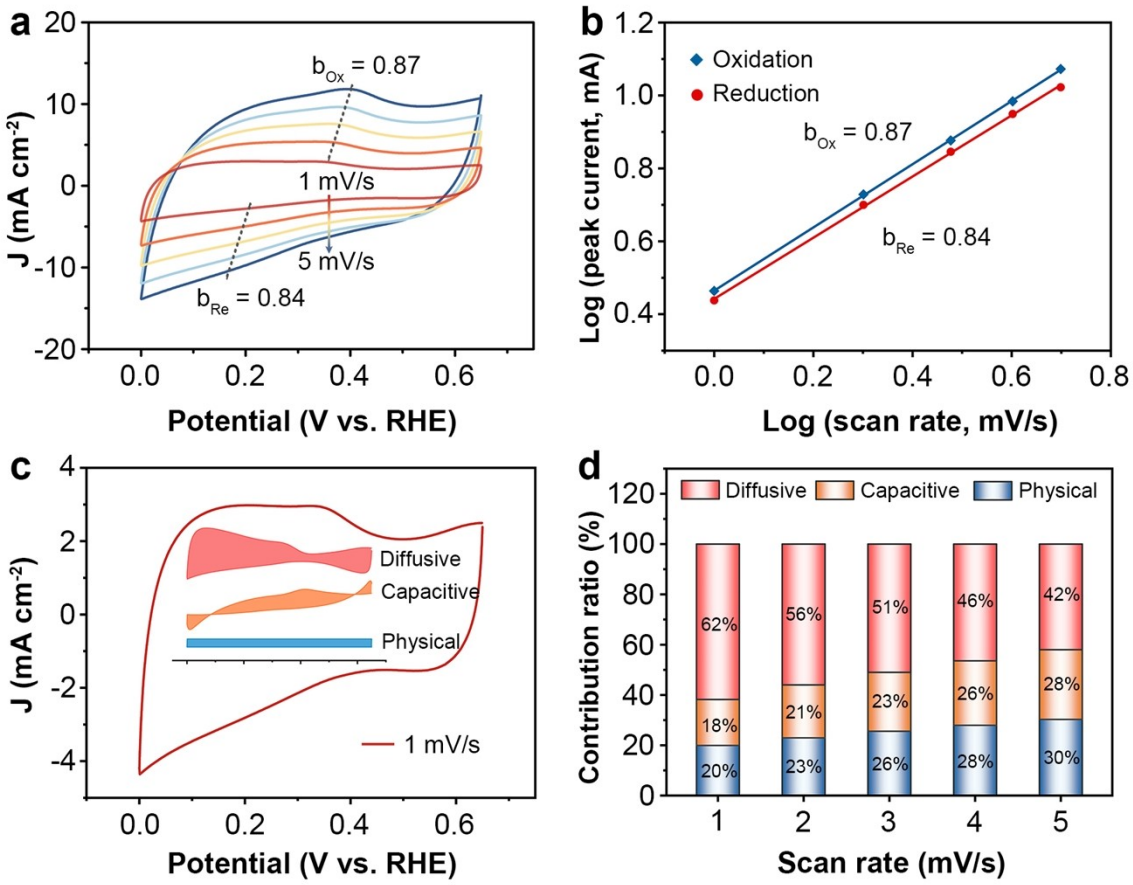

Fig. S25 Capacitance analysis of MSN-WO_{3-x}. (a) CV curves recorded at various scan rates with calculated b values. Scan rates vary from 1 to 5 mV/s. (b) Analysis of b value for reduction and oxidation peaks. (c) Capacitive contribution at 1 mV/s. (d) Capacitive contribution at various scan rates.

The kinetics of hydrogen intercalation/extraction was evaluated by the equation: $i = av^b$, (a: adjustment coefficient, b: kinetic analysis parameter, i: current response, v: scan rate).[10, 11] A b value of 1.0 means a non-diffusion-controlled or ideal pseudocapacitive behavior and a b value of 0.5 shows diffusion-controlled kinetics. As shown in Fig. S25b, the b value of MSN-WO_{3-x} is calculated to be 0.84 and 0.87 by plotting log (v) vs. log (i) according to the reduction and oxidation peaks. The results show that MSN-WO_{3-x} features a mixed pseudo/diffusive capacitive behavior of hydrogen intercalation/extraction. In essence, both diffusive and pseudo capacity are originated from Faradic reactions, which are primarily distinct from double layer capacitance where the charge is stored through physical interaction at rough surface. However, the double layer capacitance is not distinguishable from pseudo-capacitance in Fig. S25b, so we separate the physically capacitive, pseudo-capacitive, and diffusive capacitive contributions by using the following equation: $i = k_1'v + k_1''v + k_2v^{1/2}$ (i: total current, $k_1'v$: double-layer current, $k_1''v$: pseudo-capacitive current, $k_2v^{1/2}$:diffusion-controlled current). The results show that the diffusive behavior of hydrogen intercalation/extraction dominates the CV cycle in MSN-WO_{3-x}, indicating that the hydrogen transfer in the bulk oxide is quite fast (Fig. S25d).

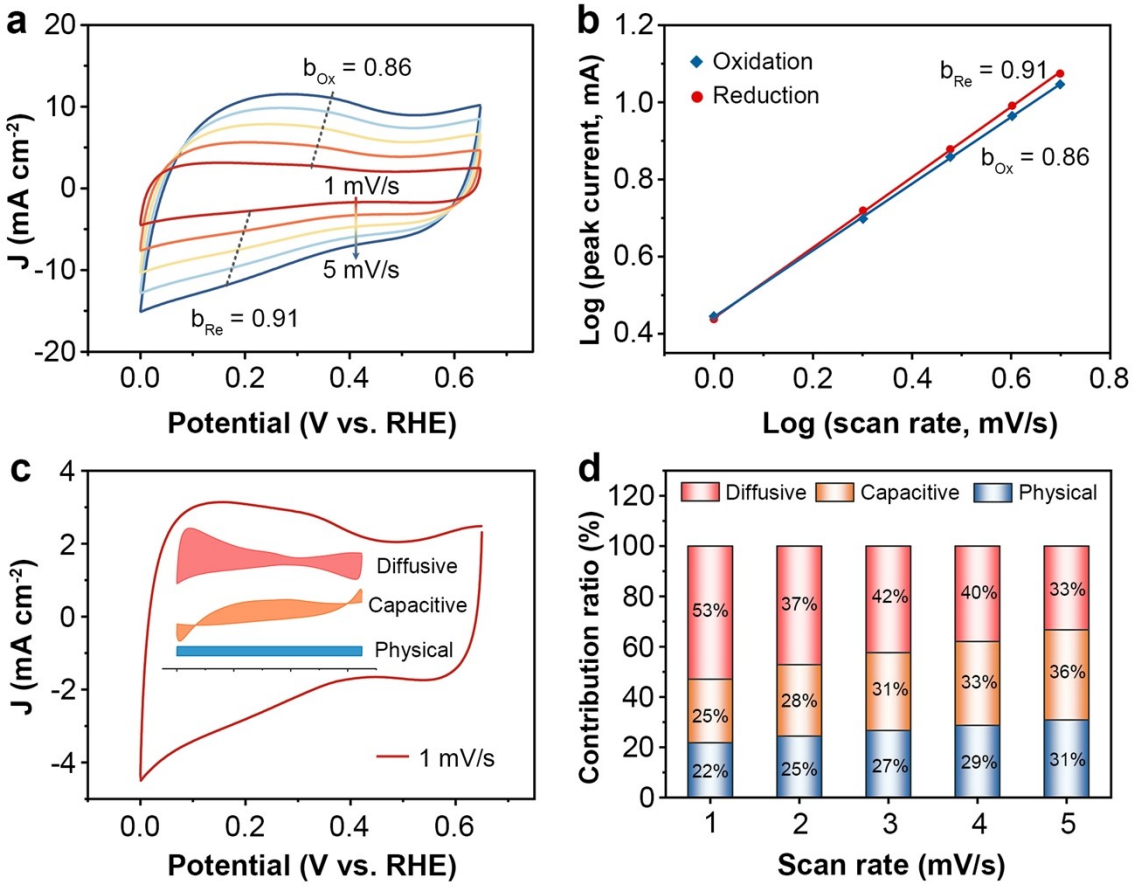

Fig. S26 Capacitance analysis of Ru/MSN-WO_{3-x}. (a) CV curves recorded at various scan rates with calculated b values. Scan rates vary from 1 to 5 mV/s. (b) Analysis of b value for reduction and oxidation peaks. (c) Capacitive contribution at 1 mV/s. (d) Capacitive contribution at various scan rates.

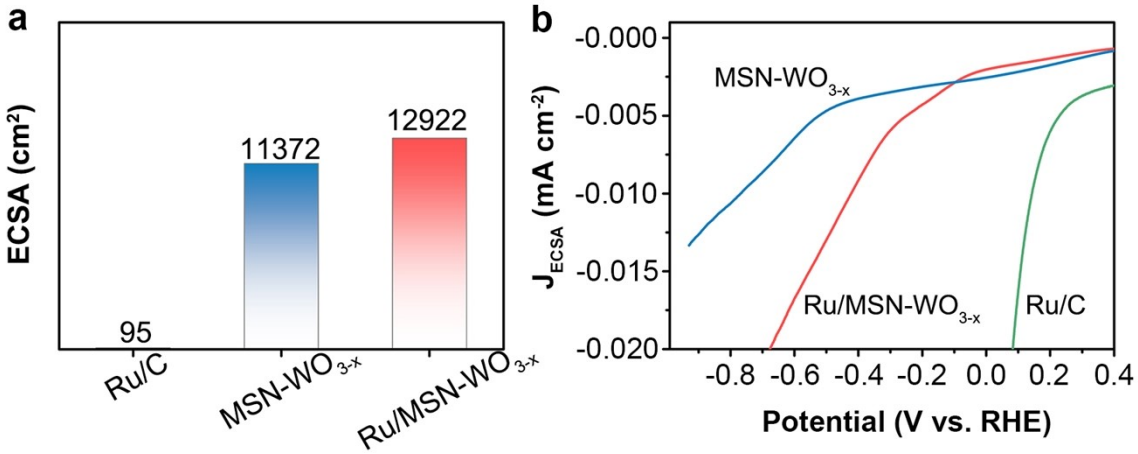

Fig. S27 (a) the ECSA values of Ru/C, MSN-WO_{3-x}, and Ru/MSN-WO_{3-x}. (b) Polarization curves normalized by the ECSA values.

The electrochemically active surface area (ECSA) was estimated by measuring the electrochemical double-layer capacitance (C_{dl}) according to the equation of ECSA = C_{dl}/C_s. C_s refers to the specific capacitance of an electrocatalyst for a flat standard with 1 cm^2 of the real surface area. In general, the specific capacitance ranges from 20 to 60 μF cm^{-2}. The average value of 40 μF cm^{-2} was usually utilized to count ECSA.[12] The high j_{ECSA} of Ru/C indicates the intrinsic catalytic activity of metallic Ru is much higher than that of MSN-WO_{3-x}, implying that the Ru cluster in Ru/MSN-WO_{3-x} is the main site for NO_3RR cycling.

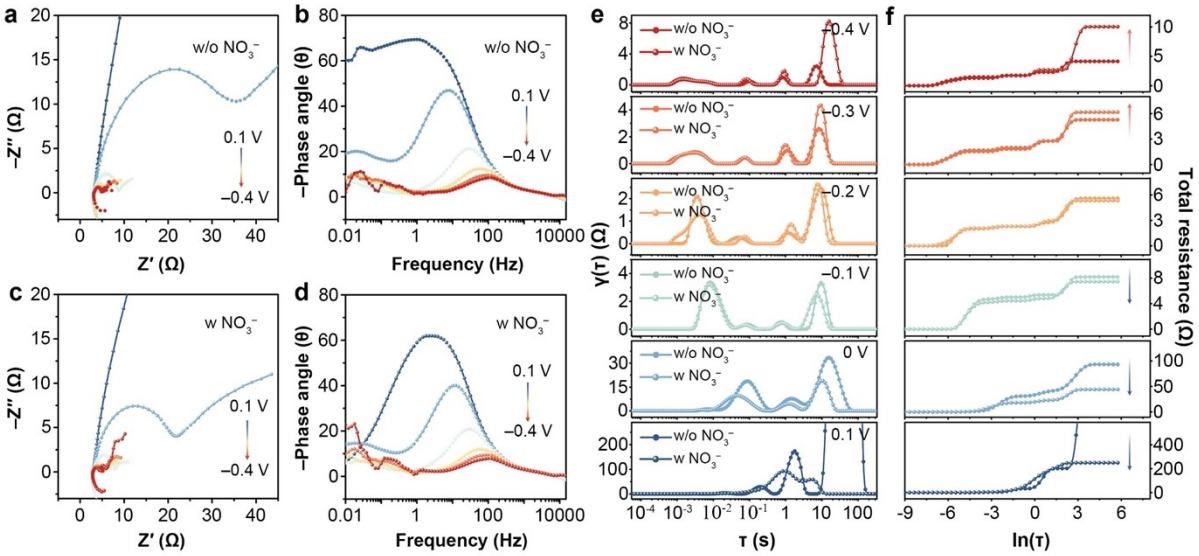

Fig. S28 Nyquist plots for Ru/C in the phosphate-buffered 0.25 M K_2SO_4 electrolyte (a) without and (c) with 0.1 M KNO_3. The corresponding Bode plots for Ru/C in the phosphate-buffered 0.25 M K_2SO_4 electrolyte (b) without and (d) with 0.1 M KNO_3. (e) The decoupled resistance distribution and (f) the corresponding total resistance computed with the imaginary part of the experiment data for Ru/C.

Note that the total resistance in the presence of NO_3^- even outweighs that in the absence of NO_3^- as the testing potential becomes more negative (below −0.2V), suggesting a strong HER competition over Ru/C at potentials relevant to HER.

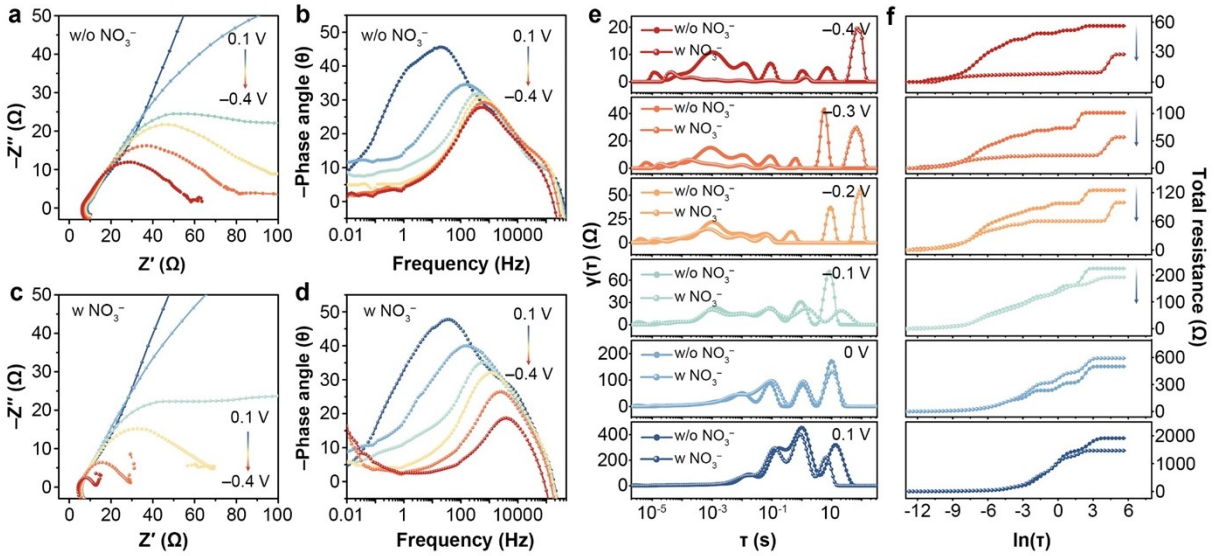

Fig. S29 Nyquist plots for MSN-WO_3 in the phosphate-buffered 0.25 M K_2SO_4 electrolyte (a) without and (c) with 0.1 M KNO_3. The corresponding Bode plots for MSN-WO_3 in the phosphate-buffered 0.25 M K_2SO_4 electrolyte (b) without and (d) with 0.1 M KNO_3. (e) The decoupled resistance distribution and (f) the corresponding total resistance computed with the imaginary part of the experiment data for MSN-WO_3.

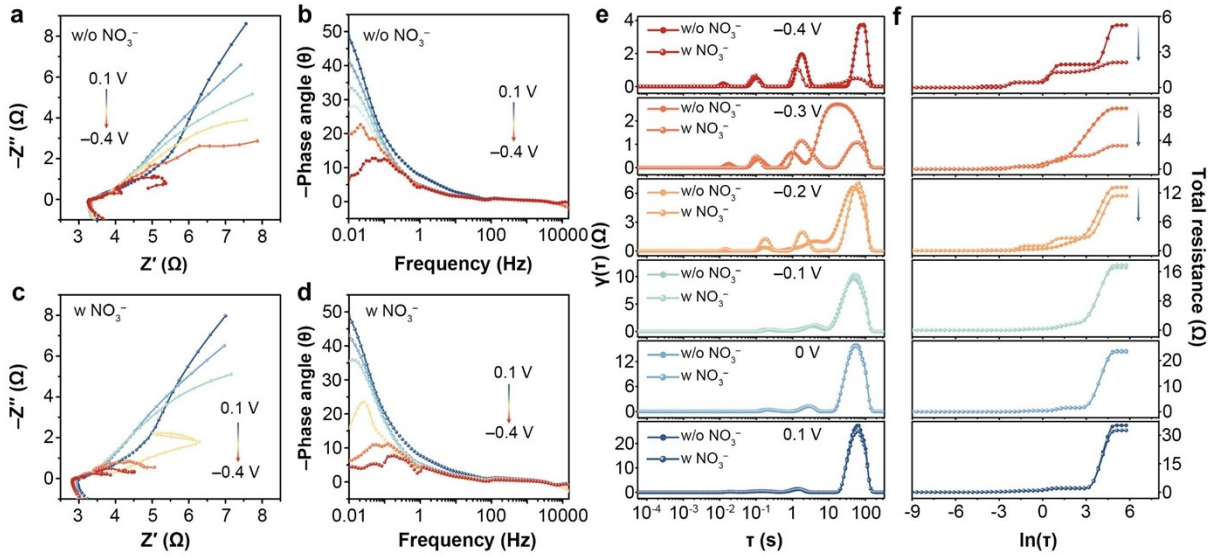

Fig. S30 Nyquist plots for MSN-WO_{3-x} in the phosphate-buffered 0.25 M K_2SO_4 electrolyte (a) without and (c) with 0.1 M KNO_3. The corresponding Bode plots for MSN-WO_{3-x} in the phosphate-buffered 0.25 M K_2SO_4 electrolyte (b) without and (d) with 0.1 M KNO_3. (e) The decoupled resistance distribution and (f) the corresponding total resistance computed with the imaginary part of the experiment data for MSN-WO_{3-x}.

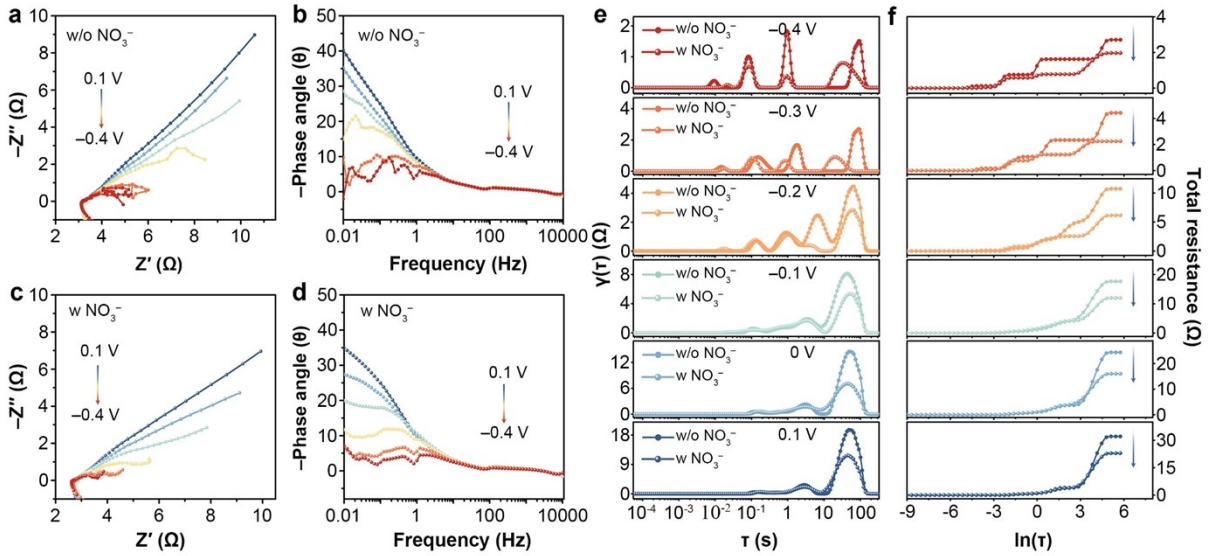

Fig. S31 Nyquist plots for Ru/MSN-WO_{3-x} in the phosphate-buffered 0.25 M K_2SO_4 electrolyte (a) without and (c) with 0.1 M KNO_3. The corresponding Bode plots for Ru/MSN-WO_3 in the phosphate-buffered 0.25 M K_2SO_4 electrolyte (b) without and (d) with 0.1 M KNO_3. (e) The decoupled resistance distribution and (f) the corresponding total resistance computed with the imaginary part of the experiment data for Ru/MSN-WO_{3-x}.

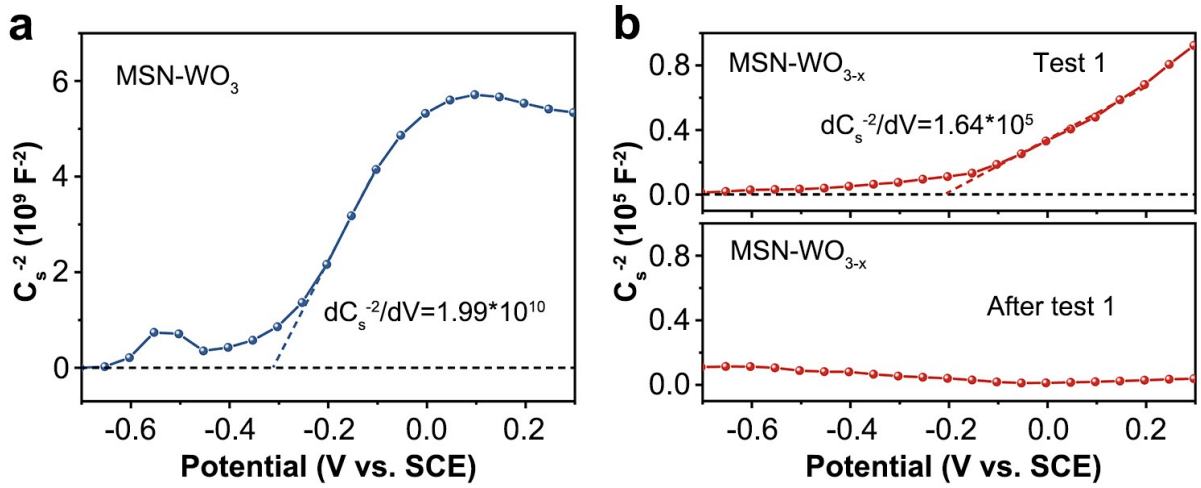

Fig. S32 Analysis of electrode surface properties. Mott-Schottky (M-S) plots of (a) MSN-WO_3 and (b) MSN-WO_{3-x}.

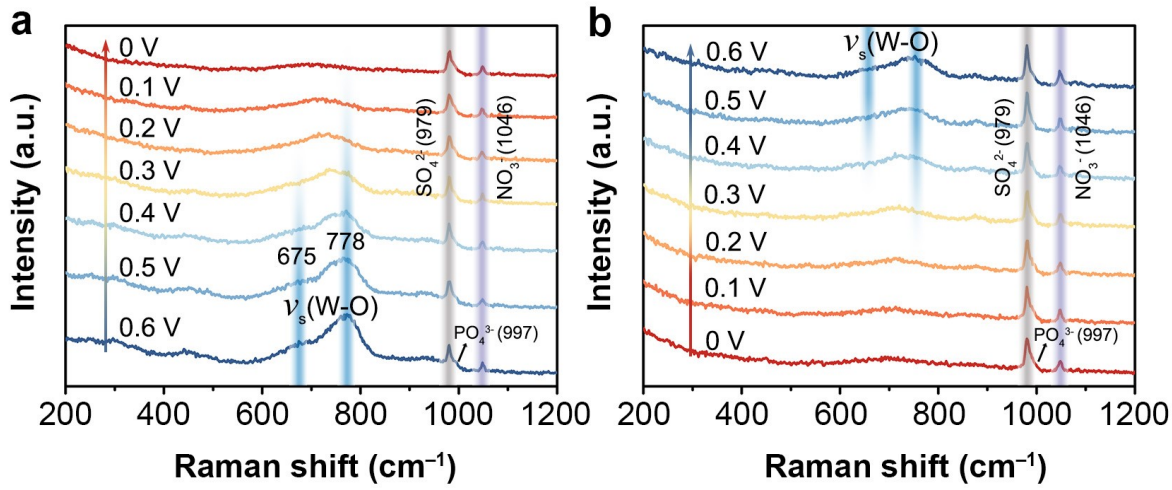

Fig. S33 (a) In-situ Raman absorption spectra of Ru/MSN-WO_{3-x} recorded from 0.6 to 0 V vs. RHE (H intercalation process). (b) In-situ Raman absorption spectra of Ru/MSN-WO_{3-x} recorded from 0 to 0.6 V vs. RHE (deprotonation process).

The bands about 675 and 778 cm^{-1} are associated with the stretching vibrations of W-O. As the potential decreased, the gradually weakened v_s(W-O) indicates that hydrogen intercalation occurs in WO_{3-x} in response to the cathodic voltage, where the H atoms are incorporated into the Brønsted acidic W-OH groups. In this regard, the in-situ H intercalation induced structural alteration could contribute to NO_3RR performance.

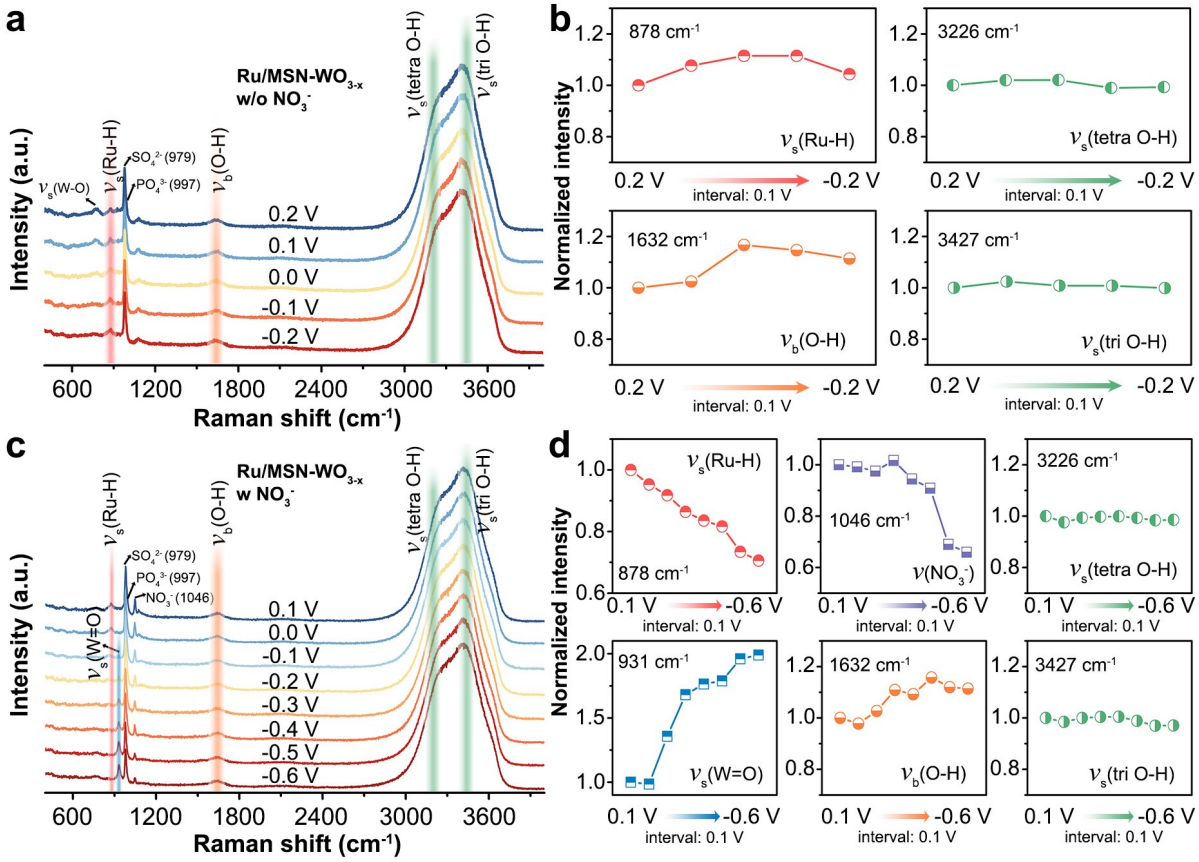

Fig. S34 (a) In-situ SERS of Ru/MSN-WO_{3-x} and (b) corresponding normalized intensity of ν_s(Ru-H), ν_b(O-H), ν_s(tetra O-H), and ν_s(tri O-H) signals under different potentials in the phosphate-buffered 0.25 M K_2SO_4 electrolyte without 0.1 M KNO_3. (c) In-situ SERS of Ru/MSN-WO_{3-x} and (d) corresponding normalized intensity of ν_s(Ru-H), ν_s(W=O), ν(NO_3^-), ν_b(O-H), ν_s(tetra O-H), and ν_s(tri O-H) signals under different potentials in the phosphate-buffered 0.25 M K_2SO_4 electrolyte with 0.1 M KNO_3.

The peak at 878 cm^{-1} is associated with the stretching vibrations of Ru-H. In the absence of NO_3^- (Fig. S34a), and the obvious response of ν_s(Ru-H) at 0.2 V vs. RHE suggests the intercalated H in H_yWO_{3-x} matrix could move toward Ru sites since a distinct signal is observed at rather low potentials (below 0 V vs. RHE) in that of pure Ru (Fig. S35a). Note that the signal of ν_s(Ru-H) progressively weakens over the whole potential range (0.1 to -0.6 V vs. RHE), which illustrates that the Ru/MSN-H_yWO_{3-x} depleted surface Ru-H species during NO_3RR process (Fig. S34c).

The peak at 931 cm^{-1} is associated with the stretching vibrations of W=O. In the presence of NO_3^-, ν_s(W=O) appears at -0.1 V vs. RHE, and increases further decreasing potential (-0.2 to -0.6 V vs. RHE), which indicates the deprotonation of WO-H species as NO_3RR proceeds. In Fig. S36a, ν_s(W=O) appears at a much lower potential of -0.3 V vs. RHE, which indicates Ru sites accelerate the deprotonation process of the H_yWO_{3-x} matrix.

The peaks at 979, 997, and 1046 cm^{-1} are associated with the S-O-S stretching mode of SO_4^{2-}, P-O-P stretching mode of PO_4^{3-}, and N-O-N stretching mode of NO_3^-, respectively. As the potential decreases, the gradually weakened signal of ν(NO_3^-) could be associated with the electrostatic repulsion under negative potentials. Such electrostatic repulsion may not favor the adsorption NO_3^- on the catalyst surface, resulting in an unsatisfactory FE of NH_3. Actually, at the potentials below -0.7 V vs. RHE, all signals gradually weaken due to the interference of H_2 bubbles.

The peak of 1632 cm^{-1} is associated with the H-O-H bending mode of water. The red shift of ν_b(O-H) from 1638 cm^{-1} (Fig. S35) to 1632 cm^{-1} suggests weaker hydrogen-bond interactions between interfacial water and Ru/MSN-H_yWO_{3-x}, which benefits for subsequent water dissociation process.

The peaks of 3226 and 3427 cm^{-1} are ascribed to the symmetric four-bonded O-H and the asymmetric three-bonded O-H stretching vibrations, respectively.

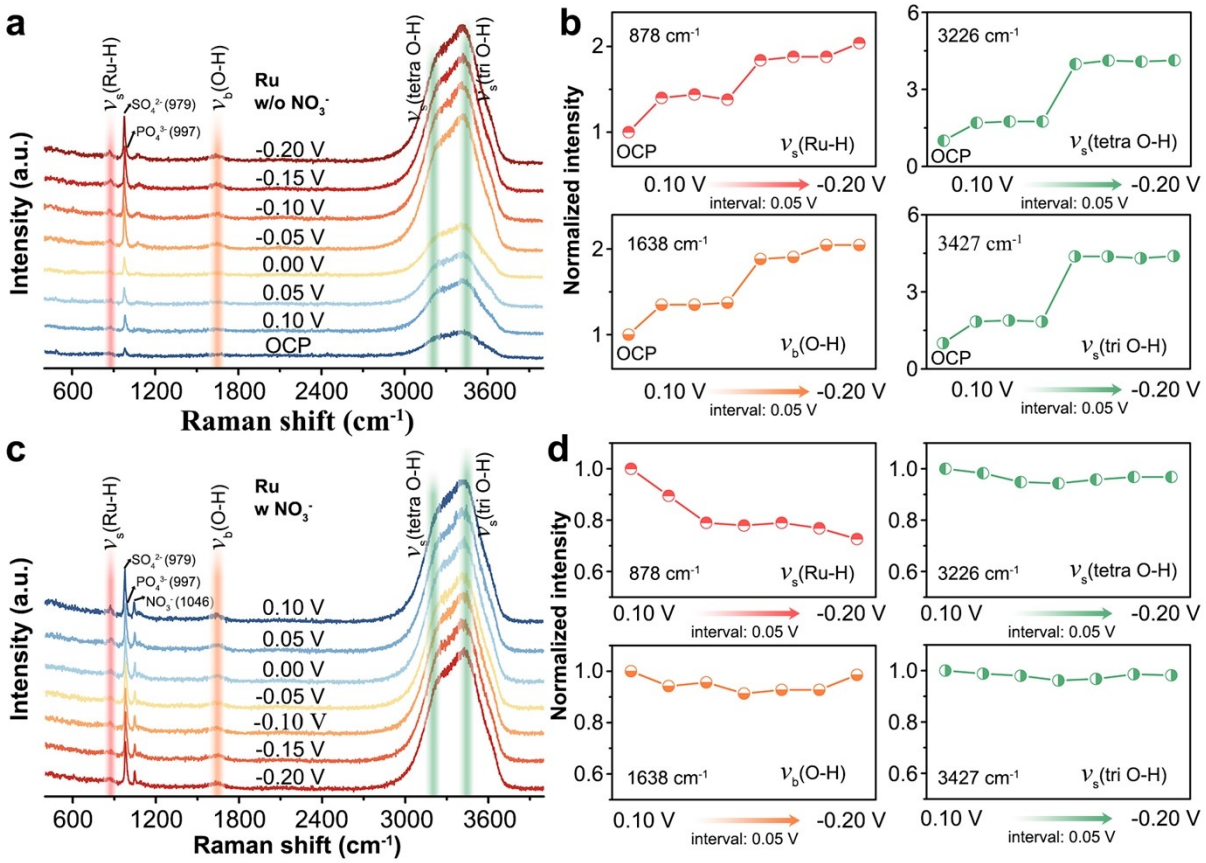

Fig. S35 In-situ SERS of Ru and corresponding normalized intensity of ν_s(Ru-H), ν_b(O-H), ν_s(tetra O-H), and ν_s(tri O-H) signals under different potentials in the phosphate-buffered 0.25 M K_2SO_4 electrolyte (a, b) without and (c, d) with 0.1 M KNO_3.

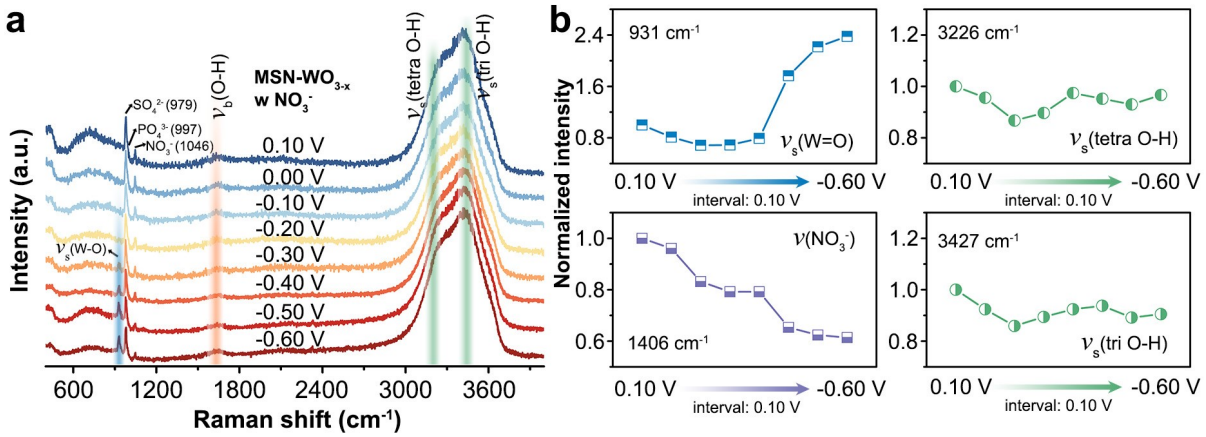

Fig. S36 (a) In-situ SERS of MSN-WO_{3-x} and (b) corresponding normalized intensity of ν_s(W=O), ν(NO_3^-), ν_s(tetra O-H), and ν_s(tri O-H) signals under different potentials in the phosphate-buffered 0.25 M K_2SO_4 electrolyte with 0.1 M KNO_3.

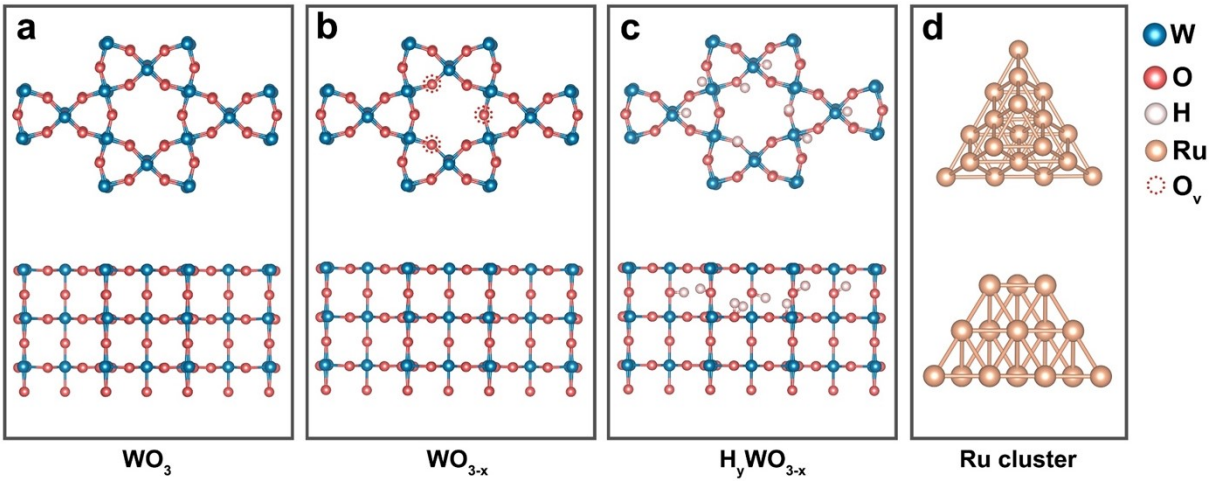

Fig. S37 Side and top view illustrations of (a)WO_3, (b) WO_{3-x}, (c) H_yWO_{3-x}, and (d) Ru cluster used in DFT calculations.

The lattice parameter used for hexagonal WO_3 was 7.504 Å × 7.504 Å × 7.721 Å (Fig. S37a). For WO_{3-x} (Fig. S37b), the oxygen vacancy was built by removing three oxygen atoms of surface of WO_3 (12.5% concentration for O atom), which is close to W^{5+} concentration (12.9%) of Ru/H_yWO_{3-x} in XPS results. As hydrogen intercalation occurs on WO_{3-x}, a moderate amount of H was added into the as-built WO_{3-x} model to simulate the actual situation, as shown in Fig. S37c.

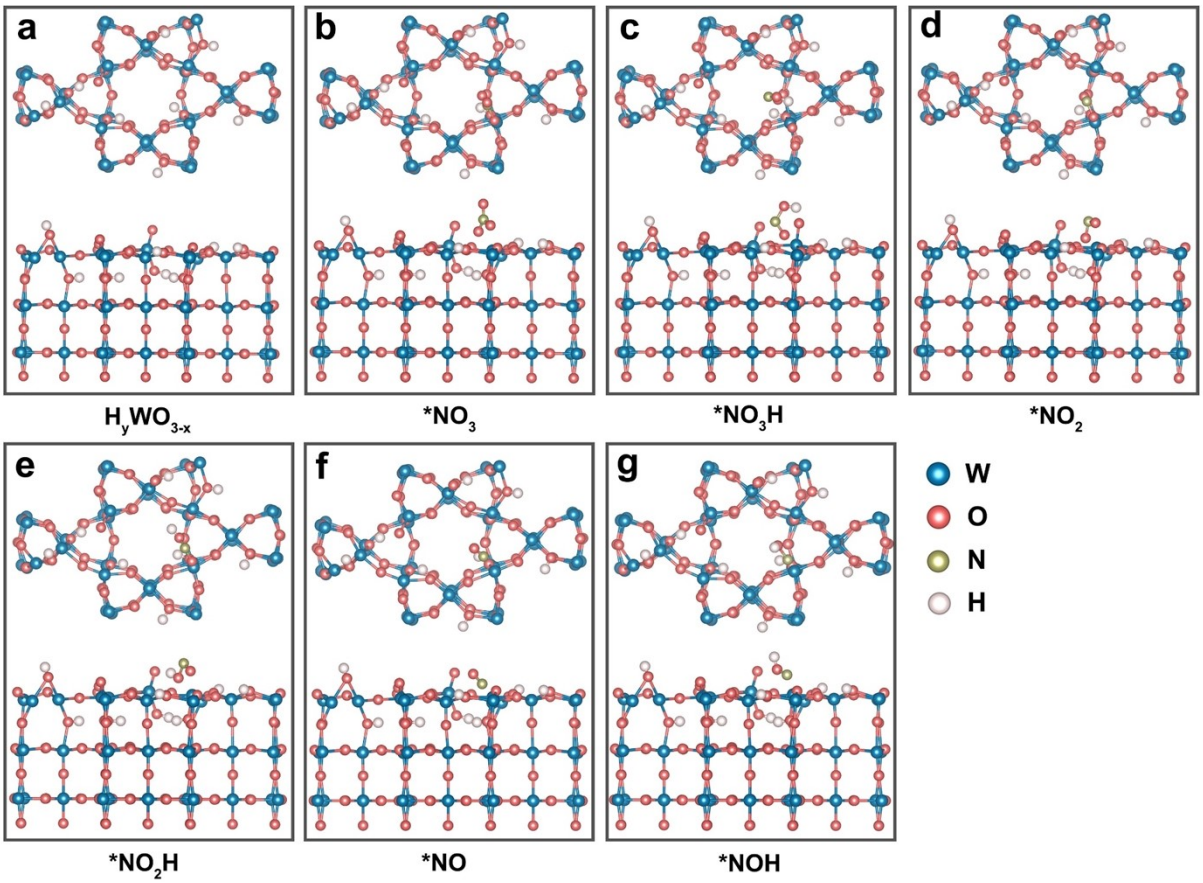

Fig. S38 Side and top view illustrations of DFT models used for calculating deoxygenation free energies of different intermediates on the H_yWO_{3-x} surface.

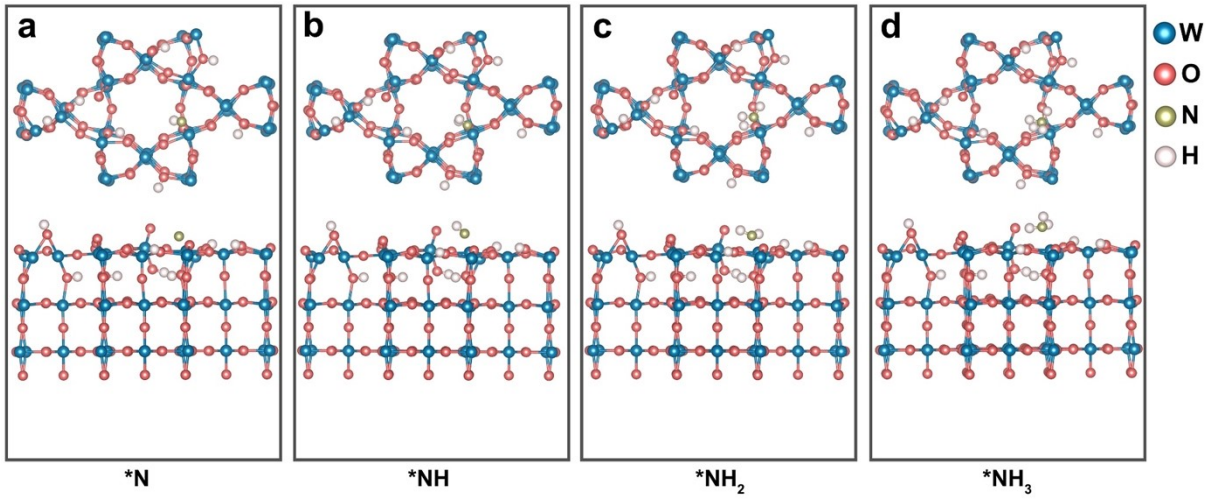

Fig. S39 Side and top view illustrations of DFT models used for calculating hydrogenation free energies of different intermediates on the H_yWO_{3-x} surface.

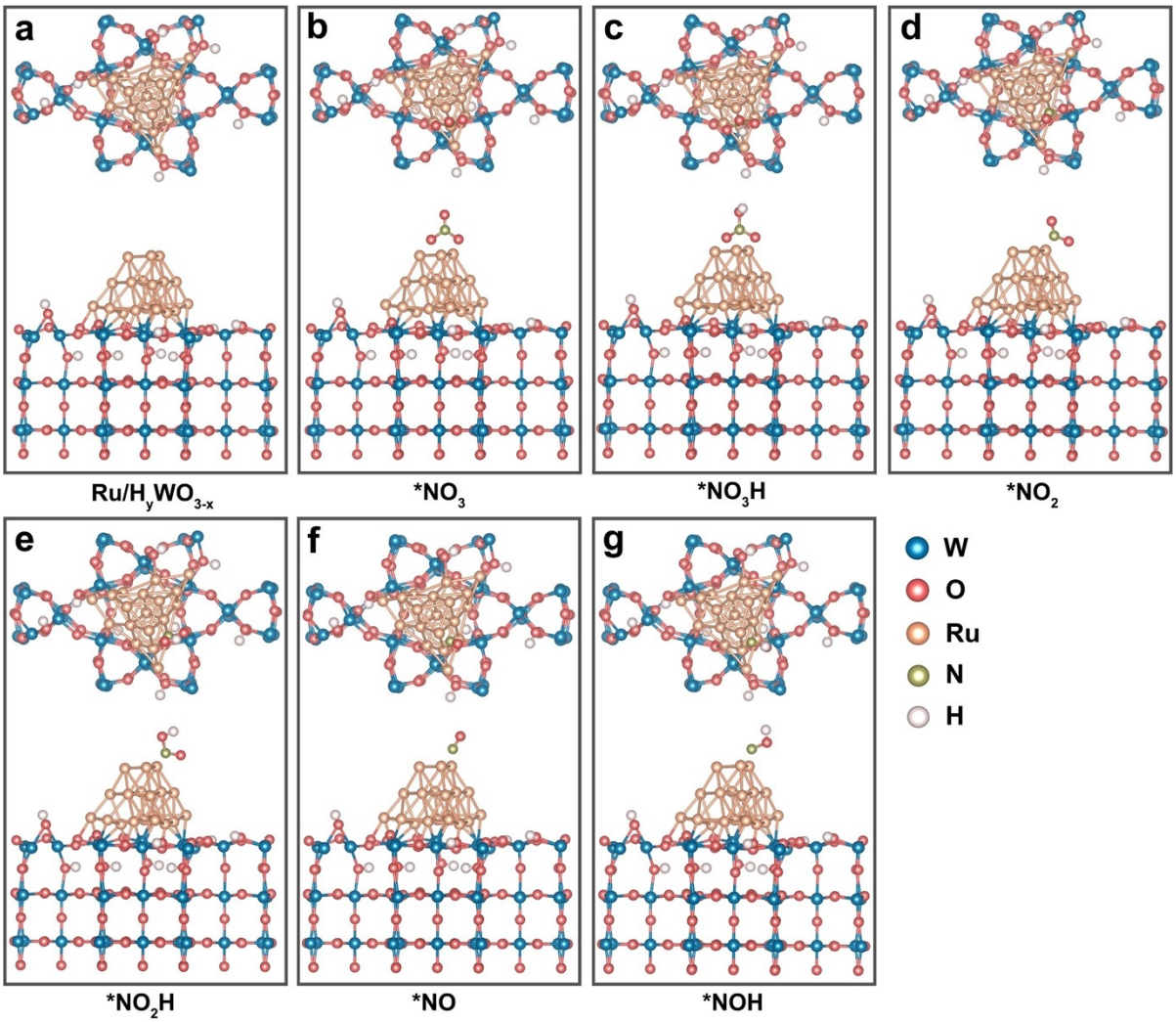

Fig. S40 Side and top view illustrations of DFT models used for calculating deoxygenation free energies of different intermediates on the Ru/H_yWO_{3-x} surface.

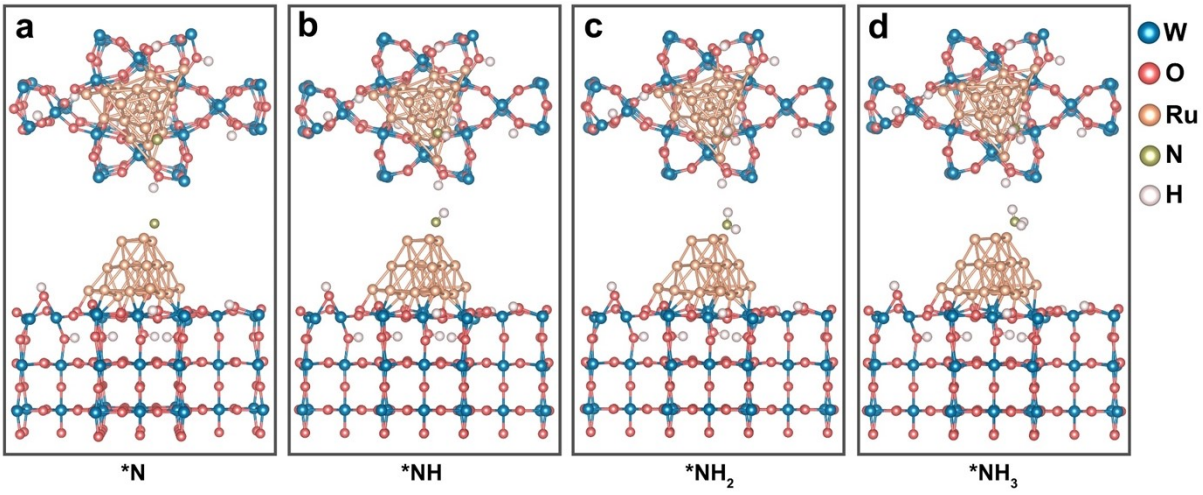

Fig. S41 Side and top view illustrations of DFT models used for calculating hydrogenation free energies of different intermediates on the Ru/H_yWO_{3-x} surface.

Table S1. Comparison of electrochemical nitrate reduction performance of the Ru/MSN-WO_{3-x} with other representative electrocatalysts in neutral solution.

Catalyst	Substrate	Catalyst loading (mg cm^{-2})	Electrolytes	Tafel slope (mV dec^{-1})	Potential (V vs RHE)	NH_3 FE	NH_3 yield rate	Refs
Co CNP	NF[a]	/	0.02 M Na_2SO_4 + 100 ppm N-NO_3^-	286	–0.49	~65%	~0.12 mg h^{-1} cm^{-2}	13
					–0.69	92.0%	0.29 mg h^{-1} cm^{-2}	
					–0.89	~76%	~0.43 mg h^{-1} cm^{-2}	
Fe CNS	NF	/	0.02 M Na_2SO_4 + 100 ppm N-NO_3^-	264	–0.57	78.4%	0.19 mg h^{-1} mg^{-1}	14
Co-Fe@Fe_2O_3	NF	4.0	0.1 M Na_2SO_4 + 500 ppm N-NO_3^-	70.73	–0.55	~60%	~0.12 mg h^{-1} cm^{-2}	15
					–0.75	85.2%	0.90 mg h^{-1} cm^{-2}	
					–0.95	~68%	~1.5 mg h^{-1} cm^{-2}	
CuPd/CN	CF[b]	2.5	0.5 M K_2SO_4 + 200 ppm N-KNO_3	/	–0.26	~45%	~0.85 mg h^{-1} cm^{-2}	16
					–0.46	96.16%	3.85 mg h^{-1} cm^{-2}	
					–0.66	~50%	~3.19 mg h^{-1} cm^{-2}	
Pd-NDs/Zr-MOF	CP[c]	0.4	0.1 M Na_2SO_4 + 500 ppm NO_3	/	–1.3	58.1	4.88 mg h^{-1} mg_{cat}^{-1}	17
Fe SAC	GC[d]	0.4	0.1 M K_2SO_4 + 0.5 M KNO_3	/	–0.50	~40%	~0.2 mg h^{-1} cm^{-2}	18
					–0.66	76%	2.0 mg h^{-1} cm^{-2}	
					–0.85	~66%	~7.6 mg h^{-1} cm^{-2}	
FOSP-Cu-0.1	CFP[e]	/	0.5 M Na_2SO_4 + 0.1 M KNO_3	/	–0.266	93.91%	1.72 mg h^{-1} cm^{-2}	19
Mo/H-CuW	CC[f]	0.25	0.5 M Na_2SO_4 + 0.05 M $NaNO_3$	/	–0.4	~24%	~0.08 mg h^{-1} cm^{-2}	20
					–0.7	94.60%	1.46 mg h^{-1} cm^{-2}	
					–1.0	~82%	~2.5 mg h^{-1} cm^{-2}	
Cu@Cu_2O MSs	CP	0.4	0.1 M Na_2SO_4 + 500 ppm NO_3^-	/	–0.8	~70%	~0.04 mg h^{-1} cm^{-2}	21
					–1.1	80.57%	2.23 mg h^{-1} cm^{-2}	
					–1.3	~40%	~1.36 mg h^{-1} cm^{-2}	
O-Cu–PTCDA	/	13.0	0.1 M PBS + 500 ppm KNO_3	/	–0.1	~60%	~0.03 mg h^{-1} cm^{-2}	22
					–0.4	85.9%	0.44 mg h^{-1} cm^{-2}	
					–0.6	~60%	~0.8 mg h^{-1} cm^{-2}	
pCuO-10	CFP	0.5	0.05 M KNO_3 + 0.05 M H_2SO_4	/	–0.7	45%	5.68 mg h^{-1} cm^{-2}	23
CuFe-450	CP	0.5	0.1 M PBS + 3 mM NO_3^-	/	–0.8	76.1%	1.34 mg h^{-1} cm^{-2}	24
BCDs/$NiCo_2O_4$	CC	/	0.5 M K_2SO_4 +200 ppm N-NO_3^-	/	–0.55	100%	2.96 mg h^{-1} cm^{-2}	25
Cu/Cu_2O NWAs	CM[g]	/	0.5 M Na_2SO_4 + 200 ppm N-NO_3^-	/	–0.85	95.8%	4.16 mg h^{-1} cm^{-2}	26

Catalyst	Substrate	Catalyst loading (mg cm^{-2})	Electrolytes	Tafel slope (mV dec^{-1})	Potential (V vs RHE)	NH_3 FE	NH_3 yield rate	Refs
a-RuO_2	CP	/	0.5 M Na_2SO_4 + 200 ppm N-NO_3^-	/	–0.35	97.46	1.97 mg h^{-1} cm^{-2}	27
Fe/Ni_2P	CC	2.0	0.2 M K_2SO_4 + 50 mM NO_3^-	173	–0.2	~58%	~0.8 mg h^{-1} cm^{-2}	28
					–0.4	94.3%	4.17 mg h^{-1} cm^{-2}	
					–0.6	~82%	~6.5 mg h^{-1} cm^{-2}	
Cu-GS-1000	CFP	0.5	0.1 M K_2SO_4 + 0.1 M KNO_3	/	–0.8	98%	3.0 mg h^{-1} mg_{cat}^{-1}	29
TiO_{2-x}	CP	1.0	0.5M Na_2SO_4 + 50 ppm of N-NO_3^-	/	–1.6 V (vs SCE)	85.0%	0.77 mg h^{-1} cm^{-2}	30
NiPr-TPA-COF	CFP	1.0	0.5 M K_2SO_4 + 0.1 M KNO_3	/	–1.38 V (vs SCE)	~90%	~ 1.1 mg h^{-1} cm^{-2}	31
Meso-PdN NCs	CP	0.1	0.1 M Na_2SO_4 + 5.0 mM of KNO_3	227	–0.4	~62%	0.04 mg h^{-1} cm^{-2}	32
					–0.7	96.1%	0.38 mg h^{-1} cm^{-2}	
					–1.0	~25%	0.4 mg h^{-1} cm^{-2}	
Pd/TiO_2	CC	10.0	1 M LiCl + 0.25 M $LiNO_3$	217.0	–0.3	~39%	~0.02 mg h^{-1} cm^{-2}	33
					–0.5	~42%	0.2 mg h^{-1} cm^{-2}	
					–0.7	92.1%	1.12 mg h^{-1} cm^{-2}	
RuFe NFs	NF	2.0	0.5 M Na_2SO_4 + 0.1 M $NaNO_3$	/	–0.10	~87%	~0.1 mg h^{-1} cm^{-2}	34
					–0.30	92.9%	0.27 mg h^{-1} cm^{-2}	
					–0.65	85.1%	7.74 mg h^{-1} cm^{-2}	
meso-CoCu	CP	0.30	0.5 M K_2SO_4 + 0.1 M KNO_3	210	–0.50	82.0%	~5 mg h^{-1} cm^{-2}	35
					–0.65	98.8%	17.28 mg h^{-1} cm^{-2}	
					–0.70	74.1%	~13 mg h^{-1} cm^{-2}	
Zn/Cu-2.3	CP	0.28	0.5 M K_2SO_4 + 0.1 M KNO_3	/	–0.35	~79%	~9.5 mg h^{-1} cm^{-2}	36
					–0.55	98.4%	21.5 mg h^{-1} cm^{-2}	
					–0.85	~84%	~27.6 mg h^{-1} cm^{-2}	
Fe_2TiO_5	CP	0.10	PBS + 0.1 M KNO_3	120.8	–0.8	~64%	~0.7 mg h^{-1} cm^{-2}	37
					–1.0	87.5%	1.3 mg h^{-1} cm^{-2}	
					–1.2	~70%	~0.9 mg h^{-1} cm^{-2}	
$Pt_{0.9}/Ce_{0.5}$-SS	CC	2.0	0.5 M Na_2SO_4 + 0.1 M KNO_3	/	–0.2	~60%	~0.4 mg h^{-1} cm^{-2}	38
					–0.5	94.12%	5.2 mg h^{-1} cm^{-2}	
					–0.8	~69%	~10 mg h^{-1} cm^{-2}	
Cu-NiO UTNSs	CC	0.25	0.5 M Na_2SO_4 + 200 ppm NO_3^-	/	–0.7	97.2%	6.34 mg h^{-1} cm^{-2}	39

Catalyst	Substrate	Catalyst loading (mg cm^{-2})	Electrolytes	Tafel slope (mV dec^{-1})	Potential (V vs RHE)	NH_3 FE	NH_3 yield rate	Refs
RhCu M-tpp	CP	0.5	0.5 M Na_2SO_4 + 3000 ppm $NaNO_3$	/	–0.1	~69%	~0.06 mg h^{-1} cm^{-2}	40
					–0.2	84.8%	~0.16 mg h^{-1} cm^{-2}	
					–0.5	~35%	0.36 mg h^{-1} cm^{-2}	
$Cu_2Cl_2(BINAP)_2$,	CP	1.0	0.5 M K_2SO_4 + 0.1 M KNO_3	224.02	–0.646	~69%	~1.5 mg h^{-1} cm^{-2}	41
					–0.846	~81%	~4.5 mg h^{-1} cm^{-2}	
					–1.046	~90%	~7 mg h^{-1} cm^{-2}	
Fe@Cu_1FeO_x	CP	1.3	0.1 M K_2SO_4 + 1000 ppm KNO_3	/	–1.3 V (vs SCE)	95.3%	1.98 mg h^{-1} cm^{-2}	42
Ru/MSN-WO_{3-x}	NF	~40	0.25 M K_2SO_4 + 0.5 M phosphate buffer +0.1 M KNO_3	177.0	0.1	99.8%	0.06 mg h^{-1} cm^{-2}	**This work**
					0	95.1%	0.49 mg h^{-1} cm^{-2}	
					–0.1	93.8%	1.07 mg h^{-1} cm^{-2}	
					–0.2	90.9%	2.15 mg h^{-1} cm^{-2}	
					–0.3	88.8%	4.36 mg h^{-1} cm^{-2}	
					–0.4	85.7%	7.02 mg h^{-1} cm^{-2}	
					–0.5	83.7%	8.77 mg h^{-1} cm^{-2}	
					–0.6	82.4%	12.38 mg h^{-1} cm^{-2}	
Ru/C	NF	4.0	0.25 M K_2SO_4 + 0.5 M phosphate buffer +0.1 M KNO_3	203.1	0.1	64.6%	0.03 mg h^{-1} cm^{-2}	**This work**
					0	91.4%	0.09 mg h^{-1} cm^{-2}	
					–0.1	53.0%	0.22 mg h^{-1} cm^{-2}	
					–0.2	30.2%	0.35 mg h^{-1} cm^{-2}	
					–0.3	18.9%	0.44 mg h^{-1} cm^{-2}	
					–0.4	22.8%	0.76 mg h^{-1} cm^{-2}	
					–0.5	18.8%	1.16 mg h^{-1} cm^{-2}	
					–0.6	19.2%	1.96 mg h^{-1} cm^{-2}	

a. NF: nickel foam, b. CF: copper foam, c. CP: carbon paper, d. GC: glassy carbon, e. CFP: carbon fiber paper, f. CC: carbon cloth, g. CM: Cu mesh,

Table S2. Comparison of the Ru mass activity of Ru/C and Ru/MSN-WO_{3-x} for ammonia production.

Potential (V vs RHE)	**Mass activity of Ru**	
	Ru/C (Ru mass loading: 0.20 mg cm^{-2})	Ru/MSN-WO_{3-x} (Ru mass loading: 0.21 mg cm^{-2})
0.1	0.15 mg h^{-1} mg_{cat}^{-2}	0.30 mg h^{-1} mg_{cat}^{-2}
0	0.47 mg h^{-1} mg_{cat}^{-2}	2.33 mg h^{-1} mg_{cat}^{-2}
–0.1	1.11 mg h^{-1} mg_{cat}^{-2}	5.14 mg h^{-1} mg_{cat}^{-2}
–0.2	1.74 mg h^{-1} mg_{cat}^{-2}	10.26 mg h^{-1} mg_{cat}^{-2}
–0.3	2.19 mg h^{-1} mg_{cat}^{-2}	20.74 mg h^{-1} mg_{cat}^{-2}
–0.4	3.79 mg h^{-1} mg_{cat}^{-2}	33.45 mg h^{-1} mg_{cat}^{-2}
–0.5	5.79 mg h^{-1} mg_{cat}^{-2}	41.78 mg h^{-1} mg_{cat}^{-2}
–0.6	9.80 mg h^{-1} mg_{cat}^{-2}	58.97 mg h^{-1} mg_{cat}^{-2}

Note: the mass loading of Ru in Ru/MSN-WO_{3-x} was determined to be 0.21 mg cm^{-2} by ICP-OES. For better comparison, 4 mg 5wt% Ru/C was drop cast on NF to ensure the Ru/C electrode with a similar Ru mass loading.

References

1 D. Zhu, L. Zhang, R. E. Ruther and R. J. Hamers, *Nat. Mater.*, 2013, **12**, 836-841.
2 L. C. Green, D. A. Wagner, J. Glogowski, P. L. Skipper, J. S. Wishnok and S. R. Tannenbaum, *Analytical Biochemistry*, 1982, **126**, 131-138.
3 L. Wu, L. Su, Q. Liang, W. Zhang, Y. Men and W. Luo, *ACS Catal.*, 2023, **13**, 4127-4133.
4 S. Han, H. Li, T. Li, F. Chen, R. Yang, Y. Yu and B. Zhang, *Nat. Catal.*, 2023, **6**, 402-414.
5 G. Kresse and J. Furthmüller, *Phys. Rev. B*, 1996, **54**, 11169.
6 J. P. Perdew, K. Burke and M. Ernzerhof, *Phys. Rev. Lett.*, 1996, **77**, 3865.
7 G. Kresse and D. Joubert, *Phys. Rev. B*, 1999, **59**, 1758.
8 S. Grimme, J. Antony, S. Ehrlich and H. Krieg, *J. Chem. Phys.*, 2010, **132**, 154104.
9 J. K. Nørskov, J. Rossmeisl, A. Logadottir, L. Lindqvist, J. R. Kitchin, T. Bligaard and H. Jonsson, *J. Phys. Chem. B*, 2004, **108**, 17886-17892.
10 H.-S. Kim, J. B. Cook, H. Lin, J. S. Ko, S. H. Tolbert, V. Ozolins and B. Dunn, *Nat. Mater.*, 2017, **16**, 454-460.
11 J. Wang, J. Polleux, J. Lim and B. Dunn, *J. Phys. Chem. C*, 2007, **111**, 14925-14931.
12 C. Wei, S. Sun, D. Mandler, X. Wang, S. Z. Qiao and Z. J. Xu, *Chem. Soc. Rev.,* 2019, **48**, 2518-2534.
13 J. Li, M. Li, N. An, S. Zhang, Q. Song, Y. Yang, J. Li and X. Liu, *Proc. Natl. Acad. Sci. U.S.A.*, 2022, **119**, e2123450119.
14 J. Li, M. Li, N. An, S. Zhang, Q. Song, Y. Yang and X. Liu, *Proc. Natl. Acad. Sci. U.S.A.*, 2021, **118**, e2105628118.
15 S. Zhang, M. Li, J. Li, Q. Song and X. Liu, *Proc. Natl. Acad. Sci. U.S.A.*, 2022, **119**, e2115504119.
16 Y. Xu, K. Shi, T. Ren, H. Yu, K. Deng, X. Wang, Z. Wang, H. Wang and L. Wang, *Small*, 2022, **18**, 2203335.
17 M. Jiang, J. Su, X. Song, P. Zhang, M. Zhu, L. Qin, Z. Tie, J.-L. Zuo and Z. Jin, *Nano Lett.*, 2022, **22**, 2529-2537.
18 Z.-Y. Wu, M. Karamad, X. Yong, Q. Huang, D. A. Cullen, P. Zhu, C. Xia, Q. Xiao, M. Shakouri and F.-Y. Chen, *Nat. Commun.*, 2021, **12**, 2870.
19 Y. Zhao, Y. Liu, Z. Zhang, Z. Mo, C. Wang and S. Gao, *Nano Energy*, 2022, **97**, 107124.
20 D. Chen, S. Zhang, X. Bu, R. Zhang, Q. Quan, Z. Lai, W. Wang, Y. Meng, D. Yin and S. Yip, *Nano Energy*, 2022, **98**, 107338.
21 M. Jiang, Q. Zhu, X. Song, Y. Gu, P. Zhang, C. Li, J. Cui, J. Ma, Z. Tie and Z. Jin, *Environ. Sci. Technol.*, 2022, **56**, 10299-10307.
22 G.-F. Chen, Y. Yuan, H. Jiang, S.-Y. Ren, L.-X. Ding, L. Ma, T. Wu, J. Lu and H. Wang, *Nat. Energy*, 2020, **5**, 605-613.
23 R. Daiyan, T. Tran-Phu, P. Kumar, K. Iputera, Z. Tong, J. Leverett, M. H. A. Khan, A. A. Esmailpour, A. Jalili and M. Lim, *Energy Environ. Sci.*, 2021, **14**, 3588-3598.
24 R. Hao, L. Tian, C. Wang, L. Wang, Y. Liu, G. Wang, W. Li and G. A. Ozin, *Chem Catal.*, 2022, **2**, 622-638.
25 X. Lu, J. Yu, J. Cai, Q. Zhang, S. Yang, L. Gu, G. I. Waterhouse, S.-Q. Zang, B. Yang and S. Lu, *Cell Rep. Phys. Sci.*, 2022, **3**.
26 Y. Wang, W. Zhou, R. Jia, Y. Yu and B. Zhang, *Angew. Chem. Int. Ed.*, 2020, **59**, 5350-5354.
27 Y. Wang, H. Li, W. Zhou, X. Zhang, B. Zhang and Y. Yu, *Angew. Chem. Int. Ed.*, 2022, **134**, e202202604.
28 R. Zhang, Y. Guo, S. Zhang, D. Chen, Y. Zhao, Z. Huang, L. Ma, P. Li, Q. Yang and G. Liang, *Adv. Energy Mater.*, 2022, **12**, 2103872.
29 J. Leverett, T. Tran-Phu, J. A. Yuwono, P. Kumar, C. Kim, Q. Zhai, C. Han, J. Qu, J. Cairney and A. N. Simonov, *Adv. Energy Mater.*, 2022, **12**, 2201500.
30 R. Jia, Y. Wang, C. Wang, Y. Ling, Y. Yu and B. Zhang, *ACS Catal.*, 2020, **10**, 3533-3540.
31 F. Lv, M. Sun, Y. Hu, J. Xu, W. Huang, N. Han, B. Huang and Y. Li, *Energy Environ. Sci.*, 2023, **16**, 201-209.
32 L. Sun and B. Liu, *Adv. Mater.*, 2023, **35**, 2207305.
33 Y. Guo, R. Zhang, S. Zhang, Y. Zhao, Q. Yang, Z. Huang, B. Dong and C. Zhi, *Energy Environ. Sci.*, 2021, **14**, 3938-3944.
34 Y. Wang, M. Sun, J. Zhou, Y. Xiong, Q. Zhang, C. Ye, X. Wang, P. Lu, T. Feng and F. Hao, *Proc. Natl. Acad. Sci. U.S.A.*, 2023, **120**, e2306461120.
35 C. Han, L. Sun, S. Han and B. Liu, *Angew. Chem. Int. Ed.*, 2024, e202416910.
36 L. Wu, J. Feng, L. Zhang, S. Jia, X. Song, Q. Zhu, X. Kang, X. Xing, X. Sun and B. Han, *Angew. Chem. Int. Ed.*, 2023, **62**, e202307952.

37 H. Du, H. Guo, K. Wang, X. Du, B. A. Beshiwork, S. Sun, Y. Luo, Q. Liu, T. Li and X. Sun, *Angew. Chem. Int. Ed.*, 2023, **62**, e202215782.
38 D. Chen, S. Zhang, D. Yin, W. Li, X. Bu, Q. Quan, Z. Lai, W. Wang, Y. Meng, C. Liu, S. Yip, F.-R. Chen, C. Zhi and J. C. Ho, *Adv. Energy Mater.*, 2023, **13**, 2203201.
39 X.-H. Wang, Q.-L. Hong, L.-Y. Shao, Q.-G. Zhai, Y.-C. Jiang, X. Ai, Y. Chen and S.-N. Li, *Adv. Funct. Mater.*, 2024, 2408834.
40 J. Zhou, Y. Xiong, M. Sun, Z. Xu, Y. Wang, P. Lu, F. Liu, F. Hao, T. Feng, Y. Ma, J. Yin, C. Ye, B. Chen, S. Xi, Y. Zhu, B. Huang and Z. Fan, *Proc. Natl. Acad. Sci. U.S.A.*, 2023, **120**, e2311149120.
41 S.-J. Zheng, X.-Y. Dong, H. Chen, R.-W. Huang, J. Cai and S.-Q. Zang, *Angew. Chem. Int. Ed.*, 2024, e202413033.
42 B. Zhou, L. Yu, W. Zhang, X. Liu, H. Zhang, J. Cheng, Z. Chen, H. Zhang, M. Li, Y. Shi, F. Jia, Y. Huang, L. Zhang and Z. Ai, *Angew. Chem. Int. Ed.*, 2024, **63**, e202406046.